Recent Development of Electrocatalytic CO₂ Reduction Application to Energy Conversion

Feng Liang,* Kaiwen Zhang, Lei Zhang,* Yingjie Zhang,* Yong Lei, and Xueliang Sun*

Carbon dioxide (CO_2) emission has caused greenhouse gas pollution worldwide. Hence, strengthening CO_2 recycling is necessary. CO_2 electroreduction reaction (CRR) is recognized as a promising approach to utilize waste CO_2. Electrocatalysts in the CRR process play a critical role in determining the selectivity and activity of CRR. Different types of electrocatalysts are introduced in this review: noble metals and their derived compounds, transition metals and their derived compounds, organic polymer, and carbon-based materials, as well as their major products, Faradaic efficiency, current density, and onset potential. Furthermore, this paper overviews the recent progress of the following two major applications of CRR according to the different energy conversion methods: electricity generation and formation of valuable carbonaceous products. Considering electricity generation devices, the electrochemical properties of metal–CO_2 batteries, including Li–CO_2, Na–CO_2, Al–CO_2, and Zn–CO_2 batteries, are mainly summarized. Finally, different pathways of CO_2 electroreduction to carbon-based fuels is presented, and their reaction mechanisms are illustrated. This review provides a clear and innovative insight into the entire reaction process of CRR, guiding the new electrocatalysts design, state-of-the-art analysis technique application, and reaction system innovation.

1. Introduction

With the development of industries, a considerable amount of carbon dioxide (CO_2) has been produced and released into the atmosphere. The concentration of CO_2 is predicted to increase

Prof. F. Liang, K. Zhang, Prof. Y. Zhang
Faculty of Metallurgical and Energy Engineering
Kunming University of Science and Technology
Kunming 650093, China
E-mail: liangfeng@kust.edu.cn; zyjkmust@126.com
Prof. F. Liang
State Key Laboratory of Complex Nonferrous Metal Resources
Clear Utilization
Kunming University of Science and Technology
Kunming 650093, China
Dr. L. Zhang, Prof. X. Sun
Department of Mechanical and Materials Engineering
University of Western Ontario
London, Ontario N6A 5B9, Canada
E-mail: lzhan684@uwo.ca; xsun@eng.uwo.ca
Prof. Y. Lei
Institute of Physics & IMN MacroNano (ZIK)
Technical University of Ilmenau
98693 Ilmenau, Germany

in 2100 to 600 ppm, which is nearly twice as much as the current amount.[1] As an extremely disturbing greenhouse gas, CO_2 exhaust may damage the carbon balance of the atmosphere and the ecosystem. Therefore, promoting CO_2 reduction and utilization is urgent. CO_2, as a linear molecule, has large ionization energy and a small electron affinity; thus, CO_2 reduction is easier than oxidization. Numerous methods, including chemical reduction, photochemical reduction, electrochemical reduction, and biological transformations, have been applied to reduce CO_2 and improve reaction rates.[2] Among these methods, CO_2 electroreduction reaction (CRR) is more promising than others, because it effectively adjusts reaction rates and products by changing their potential, current, and electrolyte.

All CRR pathways are divided into two parts: heterogeneous and homogeneous reactions.[3] Solid–gas and solid–liquid interfaces are major reaction positions in the heterogeneous process. The electrodes (or catalysts) first bond with CO_2, and then the electrons transfer between two elements. Herein, surface structure of catalysts plays a vital role in the heterogeneous catalyst performance. For instance, the high-index surfaces contain a number of low-coordination atoms, which may possess remarkable capability on the enhancement of the CO_2 catalytic capability.[4] Homogeneous reaction is also called indirect electrolysis, wherein catalysts play the role of redox shuttle. During homogeneous reaction, catalysts first accept electrons from electrodes, entering reduced state, and then donate electrons to CO_2 in solution, returning to the initial state.[5] Herein, the kinetic inhibition of electron transfer from the electrode to the substrate is reduced.[6] By contrast, CRR has several problems: 1) compared with the double bond in ketone structures, activating CO double bond in CO_2 is difficult due to its short bond length; 2) CO_2 electron affinity is tiny, and the energy gap between the highest occupied and lowest unoccupied molecular orbitals is large, indicating that the potential transferring electrons should be negative; 3) some side reactions, such as hydrogen evolution reaction (HER), may stick to the surface of catalysts and reduce the Faraday efficiency of CRR.[7]

As one of the most critical applications of CRR, energy conversion is closely interrelated with the fundamental interests of mankind. Thus, the improvement of electrocatalysts is the vital issue of electroreduction to overcome the above difficulties

and facilitate efficient energy conversion. The application of proper catalysts is always crucial to the entire reaction. Active and selective catalysts must possess a strong CO bond energy but weak H bond energy. Varieties of catalysts, including noble metal catalysts, transition metal catalysts, organic polymer, and carbon materials, have been currently developed with the large amount of research work. The application of CRR is mainly separated into the following two parts based on the different pathways of energy conversion: metal–CO_2 batteries and electroreduction of CO_2 to fuels.

As one of the strategies of energy conversion, CO_2 is normally reduced to varieties of carbonous products, such as carbon monoxide (CO), methane, and other hydrocarbons. The entire reaction occurs in the electrolytic cell cathode, and the main reaction of the anode is the oxygen evolution reaction.[8] Furthermore, product efficiency depends on the electrode structure and reaction conditions.[9] As shown in **Figure 1**, the first CRR in electrochemistry history was performed in 1870. Royer reported the reduction of CO_2 to formic acid on Zn electrodes.[10] Gas diffusion electrodes were introduced in 1990 to increase the contact area of the gas and liquid phases and the surface of catalysts, which finally enhances catalytic

efficiency.[11] However, high cost, low product selectivity, and poor stability are still the major problems, thus industrializing the necessary CRR application.[12]

Moreover, metal–CO_2 batteries, which are another type of utilization form of CO_2 electroreduction, can convert chemical energy into electrical energy. Among all CO_2-assist batteries, metal–CO_2 batteries currently show the most potential due to the use of active metals, such as lithium, sodium, zinc, magnesium, and aluminum, as anodes. Li–CO_2 batteries are first reported, thus providing a new way of mitigating the greenhouse effect and the generation of electrical energy simultaneously. Na–CO_2 batteries were developed later, but their high energy density and cheap cathode materials always attracted considerable attention. Under similar conditions, Na–CO_2 batteries demonstrated better cycle performance than Li–CO_2 batteries.[13] Studies on other batteries may not be as mature as the two kinds of batteries but still have a promising future. Although numerous works about CRR have been conducted from the viewpoint of electrocatalysts,[14] metal–CO_2 batteries,[15] and fuel production.[16] Our review is organized from a new way by taking progress and perspective of two types of energy conversion: metal–CO_2 batteries and fuel production
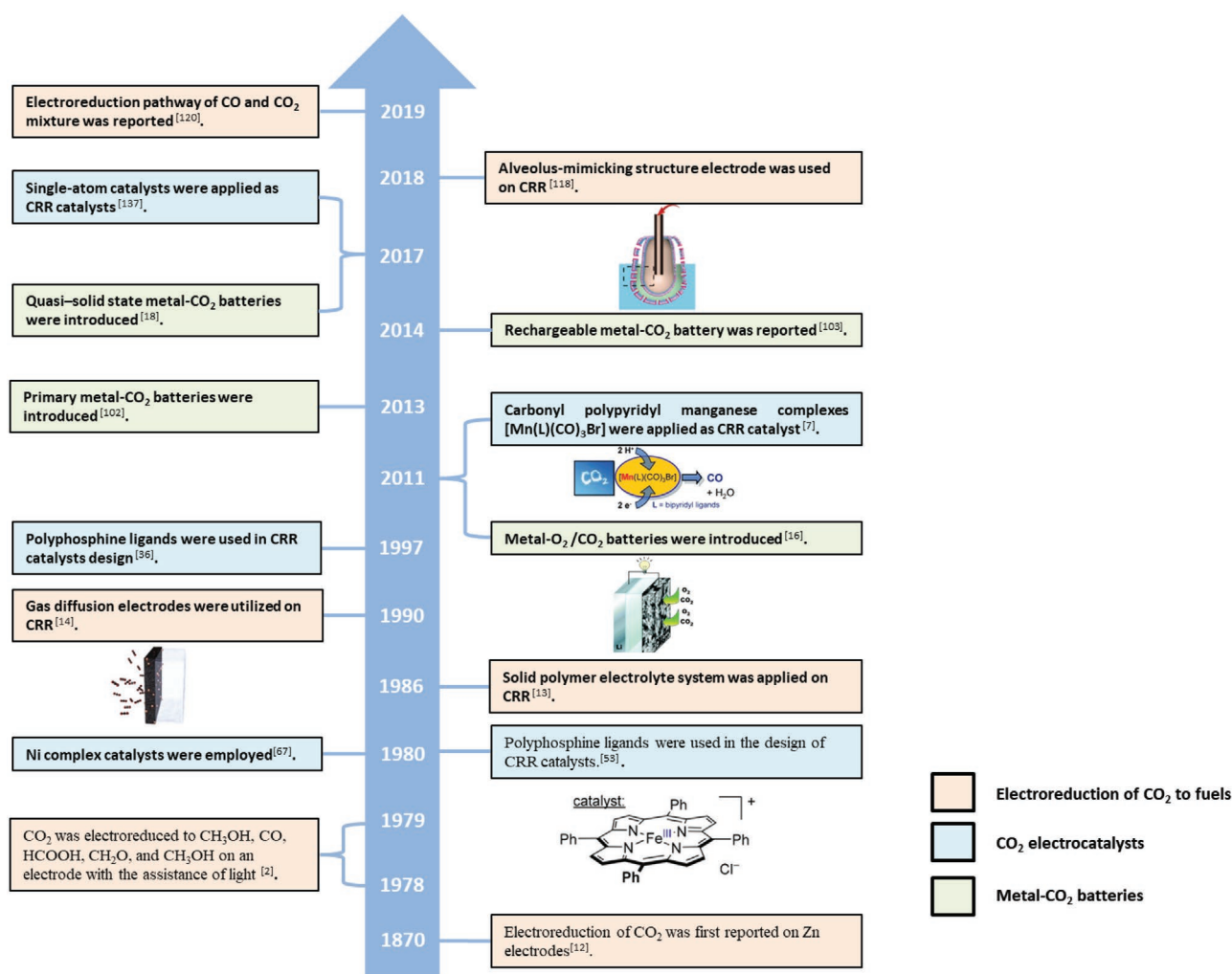

Figure 1. Milestone for the development of CO_2 electroreduction.

**ADVANCED
SCIENCE NEWS**

www.advancedsciencenews.com

NANO · MICRO
small

www.small-journal.com

as the target. Furthermore, this review elaborates four types of electrocatalysts and their application on two energy conversion forms by analyzing their reaction mechanisms, current shortcomings, and development trends. Finally, we highlight six directions of CRR development from aspects of new catalyst design, advanced analytical test method, and reaction system improvements.

2. Electrocatalysts

The common pathways of CRR involve one-, two-, four-, six-, and eight-electron reduction pathways.[4b] From the viewpoint of thermodynamics, the tendency of different electron transfer reactions is closely linked with electrode potential. Related standard redox potentials for different electron pathways are concluded in **Table 1**, which are obtained by calculating the standard Gibbs free energy of reactant in aqueous solutions. The Gibbs free energy is decided by the different pK_a of proton acceptor and proton donor.[17] As shown in Table 1, the standard redox potentials for different electron pathways have no obvious laws. This is because the whole CRR reaction process is complicated, which generally contains three steps: i) the adsorption of CO_2; ii) the surface diffusion of CO_2 and the electron and proton transformation on CO2; iii) the desorption of products. The redox potentials can be determined by many parameters, such as the electrolyte salts, CO_2 pressure, and the types of catalysts. For example, due to generation of thermodynamically unstable products, single electron transfer requires more overpotential than proton-couple multielectron transfer. It is necessary to overcome high energy barrier of adsorbing CO_2 and forming CO_2^- anion radical. Therefore, catalysts play an

important role in facilitating the reaction rate and decreasing energy gaps. The performance of four types of electrocatalysts is compared considering the activity, selectivity, price, stability, and electron conductivity. Remarkable CRR catalysts should possess six key traits as indicated in **Figure 2**.

2.1. Noble Metal and Relative Complexes

2.1.1. Nanomaterial

Compared with bulk noble metals, nanomaterials exhibit enhanced CRR catalytic capacity due to high surface area and density of low-coordinated sites.[18] From the microcosmic perspective, the activity and selectivity of noble metal electrocatalysts have a close relationship with their nanostructures. Back et al. proposed that the morphology of Au nanomaterial plays an important role in the electrocatalyst design; they found that cubic Au nanoparticles, square Au nanowires, and pentagonal Au nanowires had small dihedral angles and open planes catalyzed by CRR with high Faradaic efficiency via testing of their generalized coordination number.[19] With the aid of proximity-field nanopatterning, Jeon et al. synthesized 3D hierarchically porous gold (N/M-Au) nanostructures containing interconnected macroporous network (200–300 nm) and mesoporous (10 nm). Macroporous networks played a critical role on the transportation of ions and protons in electrolytes. Meanwhile, mesoporous endowed catalysts with large electrochemical surface areas. N/M-Au displays a high CO particle current density of 0.891 mA cm^{-2} at −0.324 mV versus RHE due to its novel structure.[20] Ag catalysts containing nanoparticles and mesoporous are proven to reduce the energy gap of the second proton transfer step, which is the rate-determining step of the entire reaction.[21] Hollow porous Ag spherical catalysts were reported to have high CO Faradaic efficiency of 94%. The density functional theory (DFT) calculation demonstrated that porous hollow structures and edge sites provide a large number of active sites.[22] Xie et al. designed a type of 3D porous Pd containing interconnected nanosheet, which had a high tendency to reduce CO_2 to formic acid. When this design was applied to the Zn–CO_2 battery, the entire battery transformed conventional discharge product carbonate into an organic liquid, thereby enhancing the cyclic performance of the battery to a large extent.[23]

Apart from surface morphology, element distribution considerably impacts the entire reaction process. Noble metals normally combine with other metals to form nanosized alloys, especially first-row transition metals, such as Cu and Sn, to enhance reaction kinetics. The optimized binding strength of intermediates is likely to form on the alloy surface due to the synergy of electronic and geometric effects.[24] Smith et al. analyzed product formation on Au–Cu bimetallic thin films via tuning composition ratio. They found that the d-band center of alloys shifted away from the Fermi level with the increase in Au content, weakening the binding energy of *CO and promoting CO desorption. Moreover, the presence of Au atoms prevented Cu atoms from oxophilicity. Afterward, relatively low *H binding energy of Cu atoms inhibited HER and enhanced the selectivity of the entire catalyst effectively.[25] Lu et al. researched a series of Pd_xCu_y bimetallic aerogels and

Table 1. Standard potential of different CO_2 electroreduction reactions.[12b]

Half-electrochemical thermodynamic reactions	Electrode potentials (V vs SHE) under standard conditions
$CO_2(g) + e^- = CO_2^{-}$ (aq)	−1.990
$CO_2(g) + 2H^+ + 2e^- = HCOOH(l)$	−0.250
$2CO_2(g) + 2H^+ + 2e^- = H_2C_2O_4(aq)$	−0.500
$CO_2(g) + 2H_2O(l) + 2e^- = HCOO^-(aq) + OH^-$	−1.078
$2CO_2(g) + 2e^- = C_2O_4^{2-}$ (aq)	−0.590
$CO_2(g) + 2H^+ + 2e^- = CO(g) + H_2O(l)$	−0.106
$CO_2(g) + 2H_2O(l) + 2e^- = CO(g) + 2OH^-$	−0.934
$CO_2(g) + 4H^+ + 4e^- = C(s) + 2H_2O(l)$	0.210
$CO_2(g) + 2H_2O(l) + 4e^- = C(s) + 4OH^-$	−0.627
$CO_2(g) + 3H_2O(l) + 4e^- = CH_2O(l) + 4OH^-$	−0.898
$CO_2(g) + 6H^+ + 6e^- = CH_3OH(l) + H_2O(l)$	0.016
$CO_2(g) + 5H_2O(l) + 6e^- = CH_3OH(l) + 6OH^-$	−0.812
$CO_2(g) + 8H^+ + 8e^- = CH_4(g) + 2H_2O$ (l)	0.169
$CO_2(g) + 6H_2O(l) + 8e^- = CH_4(g) + 8OH^-$	−0.659
$2CO_2(g) + 12H^+ + 12e^- = CH_2CH_2(g) + 4H_2O(l)$	0.064
$2CO_2(g) + 12H^+ + 12e^- = CH_3CH_2OH(l) + 3H_2O(l)$	0.084
$2CO_2(g) + 9H_2O(l) + 12e^- = CH_3CH_2OH(l) + 12OH^-$	−0.744

**ADVANCED
SCIENCE NEWS**

www.advancedsciencenews.com

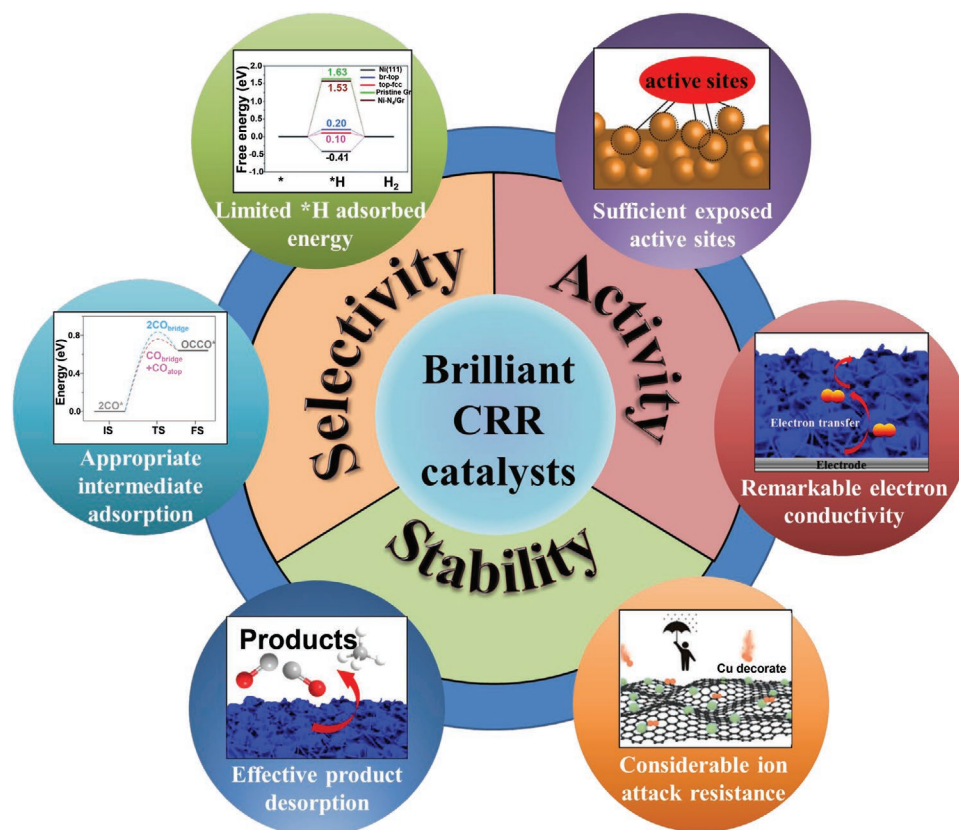NANO · MICRO

small

www.small-journal.com

Figure 2. Key traits of ideal CRR catalysts.

found that $Pd_{83}Cu_{17}$ aerogel was an ideal electrocatalyst for CRR, which produced methanol with high Faradaic efficiency up to 80%, because of the coordination of Pd and Cu with certain ratio and network structure of the aerogel.[26] Furthermore, the morphology and ratio of Pd–Cu alloy have a tremendous impact on the final products and catalytic efficiency of CRR. Notably, spherical Cu–Pd nanoalloys with a Cu/Pd molar ratio of 1/0.3 translated CO_2 into CO with high Faradaic efficiency up to 93%, but the dendritic Cu–Pd nanoalloys showed a large tendency to produce H_2. The main reason is that the d-band center of Pd played a key role in tuning the binding energy of CO and COOH intermediates, and the Cu–Pd-0.3 alloy catalyst is the most suitable ratio for balancing the d-band center.[27]

Furthermore, catalyst size control is considered to be another practical method of catalytic property improvement. For example, Sun et al. studied the CO_2 reduction performance of monodispersed Au catalysts with different sizes from 4 to 10 nm. They found that the 8 nm Au catalysts had an optimum ratio of edge site, thus showing the maximum CO FE (up to 90% at −0.67 V vs RHE). In particular, adjusting the active sites of catalysts is easy when their cluster size shrinks to the atomic level by only changing the position of small amounts of atoms.[28] Moreover, different from other catalysts, atomic-level noble metal active sites, such as Pt, Rh, and Os, display high sensitivity to surrounding coordination atoms. Herein, anchoring metal atoms on suitable substrates, such as $g-C_3N_4$, graphene, and carbon nanotubes, is a pivotal step of SAC synthesis.[29] Until now, most researchers select transition metals

as metal active sites on SACs due to the low price of transition metals. However, d-band center theory suggests that transition metals fail to maintain high activity and selectivity simultaneously during the reaction of CO_2 reduction to methanol. The main reason is that these metals have similar binding energies to *COOH and *CO, which is called scaling relation.[30] By contrast, Pt atoms anchored on graphene exhibit strong d-orbital interaction with the p-orbital of graphene, leading to deviations from the scaling relation. Thus, Jung et al. loaded Pt atoms on defective graphene with double vacancies to form Pt@dv-Gr. Compared with transition metal candidates, Pt@dv-Gr exhibited low limiting potential for methanol production. Additionally, Pt@dv-Gr showed a weaker binding of *CO than bulk Pt metal due to the lack of a Pt ensemble, which resulted in a superior methanol selectivity.[31]

2.1.2. Metal Complexes

An increasing number of molecular complexes have been applied to CRR catalysis with the development of coordination chemistry. Molecular complexes are ordinarily divided into two parts: metal center and organic ligands. The reaction pathways and binding strength of intermediates are more tunable and abundant on the surface of metal complexes than other catalysts due to the synergy of the two parts. The binding energy of optimized intermediates is efficiently enhanced by tuning the position and number of ligands, thus helping researchers to

ADVANCED
SCIENCE NEWS
www.advancedsciencenews.com

NANO · MICRO
small
www.small-journal.com

obtain their ideal products. Therefore, the selectivity and reactivity of electrocatalysts are considerably modified.[32]

Au and Ag show weak bond energy with intermediates *CO; therefore, they have a high tendency to reduce CO_2 to CO during the CRR.[36] Complexes are used to capture and transfer CO_2 via specific functional groups, such as amines.[37] Schmitt et al. prepared AgDAT from the mixture of 3,5-diamino-1,2,4-triazole (DAT) and Ag_2SO_4. Compared with bared Ag, the additional DAT weakens the bond with CO and then increases the rate of CO production, which was observed by in situ surface-enhanced Raman spectroscopy.[38] Kim et al. loaded amine molecules on Ag nanoparticles with oleylamine for capping (OLA Ag/C). Compared with other nanoparticles, the amine-capped Ag Nanoparticles maintained high CO Faradaic efficiency to 94.2% (**Figure 3**a) without increasing HER activity (Figure 3b)due to amine modification.[33] Natalie et al. found that $Au_{25}(SR)_{18}q$ ($q = -1$, 0, +1) lost a ligand and became $Au_{25}(SR)_{17}q$ or $Au_{25}S(SR)_{17}q$ to improve its catalytic capability and suppress HER, and $Au_{25}S(SR)_{17}q$ was formed by removing ligand CH_3 (Figure 3c), thereby exhibiting good selectivity and stability on CRR. The removal of ligand CH_3 using DFT exposed additional S atoms as active sites, contributing to *COOH intermediates with high stability (Figure 3d). Therefore, $Au_{25}S(SR)_{17}q$ effectively reduced CO_2 into CO and suppressed the HER.[34]

Ru complex is a kind of active electrocatalyst for CRR, and the coordination of ligand and Ru metal sites efficiently transfers electrons to CO_2. The simple methyl substituent of [Ru(tBu$_3$tpy) (bpy)(NCCH$_3$)]$^{2+}$ (2^{2+}) catalyzes the disproportionation of CO_2 to form CO_3^{2-} and CO. Moreover, CO_2 was found to bond with the surface of 2^{2+} after the one-electron transfer to 2^{2+} by employing infrared radiation (IR) spectroscopy and gas chromatography (GC) analysis. This phenomenon proved the appearance of the product and the occurrence of a second electron,

thus resulting in low overpotential coordination with high Faradaic efficiency.[39] Hadadzadeh et al. clarified the detailed pathways, in which CO_2 was electroreduced to CO on the surface of [Ru(dmbpy)(tptz)(Cl)](PF$_6$) (where dmbpy = 4,4′-dimethyl-2,2′-bipyridine, and tptz = 2,4,6-tris(2-pyridyl)-1,3,5-triazine) with DFT calculation. They further observed that a two sequential one-electron reduction process took place first and formed [Ru^{II}(dmbpy)(tptz^{2-})(Cl)]$^-$ intermediates, and then Cl$^-$ was altered by CO_2 to generate [Ru^{II}(dmbpy)(tptz)($CO_2{}^{2-}$)]. The third and fourth electronic transfers occurred on the tptz and dumbpy ligands, respectively, to generate [Ru^{II}(dmbpy$^-$)(tptz$^-$) ($CO_2{}^{2-}$)]$^{2-}$ (Figure 3e). The oxide on the coordinated-CO_2 ligand moved to combine with the free dissolved CO_2, leading to the substitution of coordinated-CO_2 and coordinated-CO ligands. Finally, CO was separated from the complex and completed the entire electrocatalytic cycle.[35] Szkaradek et al. described that graphene-supported Ru-porphyrin exhibited large activity to translate CO_2 into methane because Ru formed strong interactions with CO intermediate and then produced hydrocarbons. Furthermore, by analyzing Bader population of graphene supported porphyrin-CO_2 system, there was not obvious electron donation appearing on the graphene sheet, although graphene sheet was reported to affect elementary step energy significantly. Herein the graphene supporter only played the role of orbital polarization at the macrocyclic compound.[40]

2.2. Transition Metal and Relative Compounds

2.2.1. Fe, Co, and Ni

Fe, Co, and Ni, as the group VIII metals, have similar atomic radius and electronic configuration. The 4s orbits of these metals
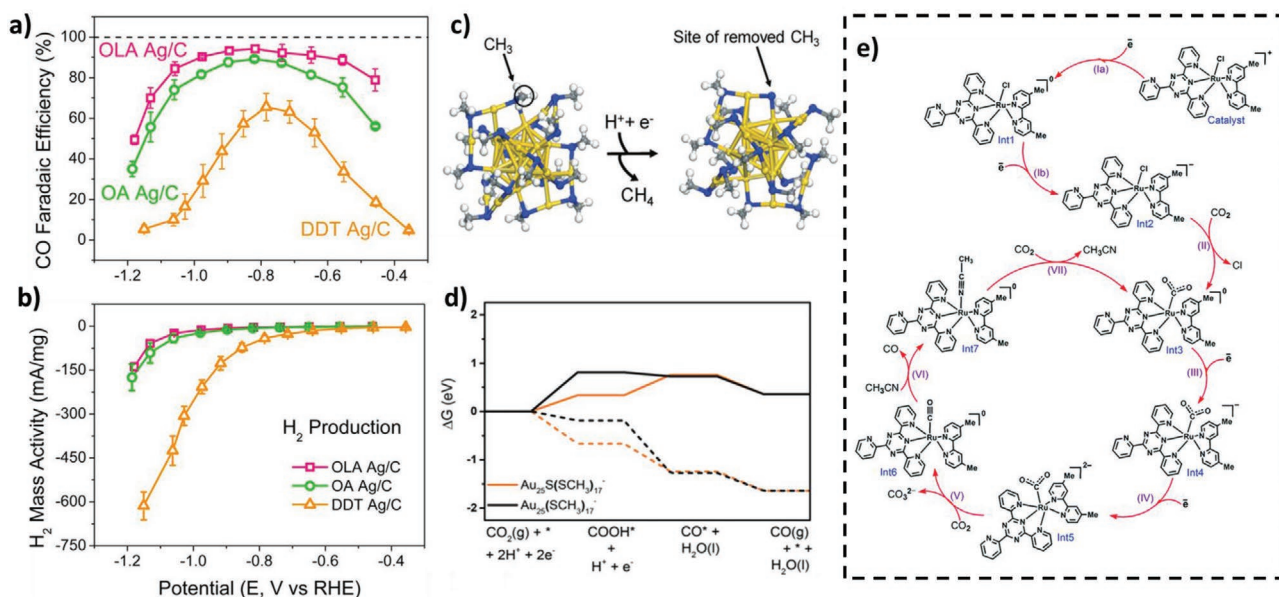

Figure 3. a) CO Faradaic efficiency and b) H_2 massive activity of Ag nanoparticles with different capping agents. Reproduced with permission.[33] Copyright 2016, American Chemical Society. c) Schematic for the reduction of the fully ligand-protected NC ($Au_{25}(SR)_{18}q$) to $Au_{25}S(SR)_{17}q$. d) Free energy diagrams for the reduction of CO_2 to CO on $Au_{25}S(SR)_{17}q$. Reproduced with permission.[34] Copyright 2018, Royal Society of Chemistry. e) mechanism for the electrocatalytic reduction of CO_2 on [Ru(dmbpy)(tptz)(Cl)](PF$_6$). Reproduced with permission.[35] Copyright 2016, Royal Society of Chemistry.

are filled, and empty orbits only exist on their 3d orbits, which are close to the Fermi level. The condition of d states is of utmost importance on the entire catalysis process. All three metals exhibit a high tendency on H₂ evolution, indicating that bulk metals without any treatment are unfavorable candidates to CRR catalysis.[41] Metal–N–C (Metal = Fe, Co, Ni) catalysts with high CO selectivity are widely used to deal with above-mentioned problems. Different electronegativity of metal, nitrogen, and carbon, leads to the shift of metal d-band center, further enhancing selectivity and activity of these metals. From the DFT analysis of Metal–N–C (Metal = Fe, Co, Ni), it has been suggested that Co–N–C displays high tendency to HER and high energy barrier of CO generation, Ni–N–C needs large overpotential to adsorb *CO but have great ability to inhibit HER. Fe–N–C displays relative balanced activity of HER and CRR.[11] The application of metal–N–C will be discussed in the following paragraph in detail.

Thus, conducting some treatments on bulk metal is necessary to suppress H₂ evolution and enhance the reduction capability of CO₂.[50] The continual reaction was also inhibited because of the large binding energy between the Fe surface and *CO intermediate. Moreover, the formation of iron carbide

leads to the inactivity of the Fe surface.[51] Taheri et al. developed a new Fe-based complex electrocatalyst, $[Fe_4N(CO)_{12}]^-$, in a buffered aqueous solution, which had remarkable catalytic capability to reduce CO₂ to formate. This electrocatalyst showed high Faradaic efficiency of nearly 96%, a high current density of 4 mA cm⁻², and an excellent stability after 24 h operation. DFT and infrared spectroelectrochemistry demonstrated that $[HFe_4N(CO)_{12}]^-$ intermediate played an important role during the formation of C−H bond. Moreover, the growth driving force of the C−H bond in aqueous solution indicates that the buffered aqueous solution promotes the selectivity of this catalyst.[52] Moreover, FeN₄ moieties play important roles on the reduction reaction of CO₂ to CO, which was investigated by designing a series of Fe–N–C materials containing different ratios of FeN₄ moieties and crystalline Fe. According to the mass percentage of Fe (0.5, 1.0, and 4.0) and the application of a wet impregnation step (w/d), five different Fe-based catalysts were named: Fe₄.₀d, Fe₁.₀w, Fe₁.₀d, Fe₀.₅d, and Fe₀.₅d-950. The content of FeN₄ at 100% (Fe₀.₅d) showed strong CO selectivity whose Faradaic efficiency reached 91% and low onset potential of 0.3 V (**Figure 4**a). On the contrary, crystalline Fe (Fe₁.₀w and
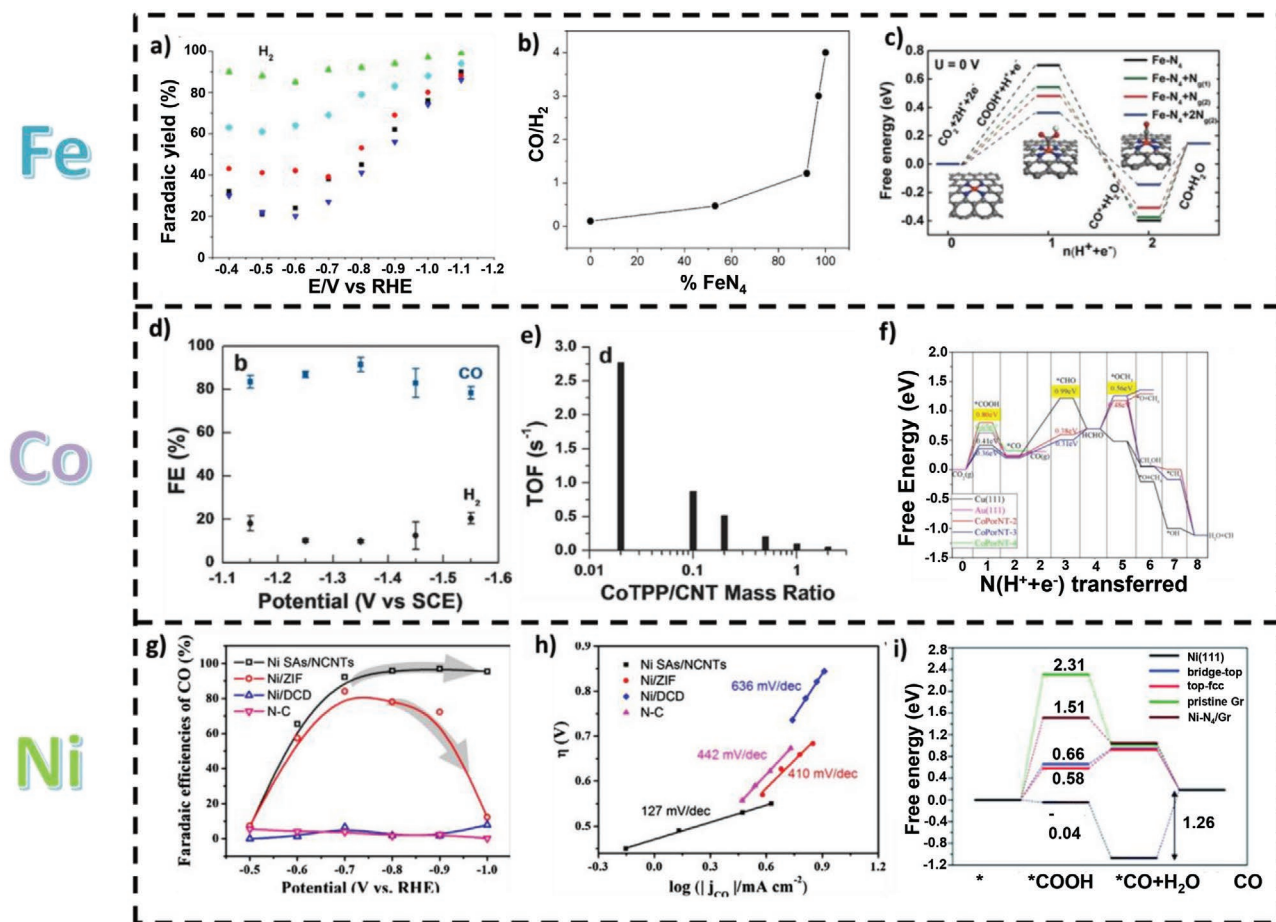

Figure 4. a) Faradaic yield for CO formation Fe₀.₀d (orange), Fe₄.₀d (green), Fe₁.₀w (cyan), Fe₁.₀d (red), Fe₀.₅d-950 (black), and Fe₀.₅d (blue). b) CO/H₂ ratio of the gas blend formed after 5 min of electrolysis at -0.5 V versus RHE. Reproduced with permission.[44] Copyright 2017, American Chemical Society. c) Free energy diagram of CRR on Fe–N₄ moieties. Reproduced with permission.[45] Copyright 2018, Wiley-VCH. d) CO Faradaic efficiency and e) TOF for CO production of CoTPP–CNT. Reproduced with permission.[46] Copyright 2017, Wiley-VCH. f) Calculated free energy diagrams of different catalysts. Reproduced with permission.[47] Copyright 2016, American Chemical Society. g) CO Faradaic efficiency and h) Tafel plots of different catalysts. Reproduced with permission.[48] Copyright 2019, Elsevier. i) the free energy diagrams for CO generation. Reproduced with permission.[49] Copyright 2018, Royal Society of Chemistry.

$Fe_{4,0}d$) is appropriate to catalyze HER. Therefore, maintaining the relative content of FeN_4 by more than 97% is a remarkable way to strengthen the CRR catalytic capability of Fe–N–C materials (Figure 4b).[44] Zhang et al. obtained atomic iron dispersed on nitrogen-doped graphene (Fe/NG) by annealing the mixture of graphene oxide and $FeCl_3$ solution at 750 °C, which showed the highest catalytic capability to reduce CO_2 to CO among all different annealing temperatures. The largest CO Faradaic efficiency was up to 80% at −0.60 V versus RHE, and the reducing current hardly demonstrated large decays. The VASP result indicated that the formation of COOH* intermediate was confirmed to be the potential limiting step of the entire reaction. Moreover, the special structure of Fe/NG, the coordination of N atom on the graphene surface, and FeN_4 moieties reduce the energy barrier to 0.29 eV (Figure 4c).[45]

HER is more likely to occur than CRR on the surface of pure Co metal. Several methods should be considered to strengthen the catalytic capability of CRR. Combining with organic elements to form complexes may be one of the effective strategies and among all complexes, CoPor is considered as the one of most ideal candidates. A type of electrocatalyst containing CoPor is called cobalt meso-tetraphenylporphyrin (CoTPP), and its major product was CO. Research showed that the immobilization of the CoTPP–carbon nanotube (CoTPP/CNT), as a heterogeneous catalyst, overcame numerous problems of homogeneous catalysts. The Faradaic efficiency dramatically improved by over 90% at −1.35 V versus SCE (Figure 4d). The turnover frequency (TOF) was reported to reach 280 h^{-1} (Figure 4e), which was 300 times larger than similar homogeneous catalysts. The unique superiority of CoTPP/CNT lies in its remarkable coordination of considerable electronic conductivity of CNT and the extraordinary catalytic capability of CoTPP. The DFT calculation confirmed that the profound stabilization of $Co^{II}TPP \cdot CO_2^-$ immediate was a vital factor in enhancing the activity of CoTPP/CNT.[46] However, the catalytic activity CoTPP was reported to drop as the reaction proceeds.[53] Jiang et al. recently took research on the mechanism of CoTPP inactivation and found two main factors. First, CoTPP was oxidized by CO_2 to form non-catalytically active $[Co^{III}TPP]OH$. Second, reductive carboxylation of porphyrin ring was likely to product $[Co^0TPP]^{2-}$ and $[Co^0TPP\text{-}CO]^{2-}$, which disrupted π-system of CoTPP and resulted in catalyst disintegration. Furthermore, bulky donating functional groups, especially OMe, have great capability to inhabit above-mentioned factors and enhance catalyst stability.[54]

Apart from CoTPP, Zhu et al. obtained cobalt–porphyrin nanotubes (CoPorNT-x, x = 2, 3, 4) by rolling different numbers of CoPor monomers. This new catalyst exhibited remarkable thermodynamically stable and unique half-metal and ferromagnetic features, thereby suggesting a potentially good candidate for CRR electrocatalysts. Furthermore, products may demonstrate numerous changes with a variety of x. The main products were methane with less overpotential than Cu catalyst in the case of x = 2, 3. However, CO became the main products with lower overpotential than Au (111) surface when x increased to 4 considering different adsorption energies of O (Figure 4f). Moreover, CoPorNT-3 showed a low proton-transfer free energy barrier and additional activity due to the high d-band center.[47]

On pure Ni electrode, H_2 and small hydrocarbon are major products of CRR.[55] Large CO_2 pressure, high temporary, and negative electrode potential substantially improve the reduction capability of CO_2.[56] $Ni\text{-}N_X$ moieties of the catalyst surface endow catalysts with high CO reduction efficiency due to the coordination of Ni and nickel-nitrogen-doped carbon (Ni-N-C) catalyst. The DFT calculation shows that all pathways of the reduction in CO_2 to CO are downhill energetics, whereas HER pathways demonstrate a considerable energy barrier. This finding shows the outstanding CO_2 catalytic capability and selectivity of Ni-N-C catalyst.[43a] Lu et al. reported that $Ni\text{-}N_x$ moieties played a pivotal role in dispersing Ni atoms on N-doped CNTs (Ni SAs/NCNTs). $Ni\text{-}N_x$ moieties also showed stable and high CO Faradaic efficiency up to 97% and low Tafel slope of 127 mV dec^{-1} (Figure 4g,h).[48] In comparison, Sun et al. synthesized N-doped carbon-supported Ni nanoparticles (Ni-NC_X@C), which manifested similar CO Faradaic efficiency up to 94% at an increased positive potential of −0.7 V versus RHE. Moreover, they found that the presence of Ni (111) in the carbon support stabilized key immediate of *COOH and increased the activity of catalysts (Figure 4i).[49]

2.2.2. Cu

Cu usually exhibits high selectivity to convert CO_2 into high-value hydrocarbons among all transition metals.[57] Among all pathways of CRR on Cu, CO often appears as an intermediate.[58] Moreover different facets of Cu nanostructures display different product selectivities. Cu (100) surface has high C_2 selectivity, and the generation of C_1 usually occurs on the Cu (111) surface.[59]

Zheng et al. reported that $CuSn_3$ was prepared via the coelectrode position process, converting CO_2 into formate. X-ray absorption studies (XAS) indicate that Sn is an electronic donor, which maintained high oxidation states in $CuSn_3$ alloy. Among various Cu_xSn_y alloys, $CuSn_3$ showed the highest formate Faradaic efficiency up to nearly 100% at −500 mV versus RHE. Moreover, $CuSn_3$ displayed higher thermodynamic limiting potentials to H_2 and CO than pure Cu and Sn, which endowed $CuSn_3$ with remarkable formate selectivity.[60] Yang et al. synthesized $Cu_{1.63}Se(1/3)$ nanoparticles in the solvent with a 1/3 volume ratio of diethylenetriamine and water. Their synthesis showed high methanol Faradaic efficiency up to 77.6% at 285 mV, and its current density reached 41.5 mA cm^{-2}. The remarkable catalytic capability of these nanoparticles was ascribed to the following points: 1) $Cu_{1.63}Se(1/3)$ had a large surface area. 2) The charge transfer resistance demonstrated that electron easily transferred on the catalyst surface. 3) The DFT data revealed that the catalyst surface generated a short $Cu_{1.63}Se(1/3)$ −CHO bond with *CHO intermediate, leading to low free energy of *CO conversion into *CHO. 4) XAS results demonstrated that the Se atom in the catalyst was unsaturated, thereby enhancing the catalytic performance.[61]

Apart from adding other elements to form alloys with Cu, tuning the morphology of the Cu-based catalyst is also a remarkable method used to improve the catalytic capability of CRR. Jiang et al. detected the C_{2+} product selectivity on Cu foil via the metal ion battery cycling method. Scanning electron

**ADVANCED
SCIENCE NEWS**
www.advancedsciencenews.com

NANO · MICRO
small
www.small-journal.com

microscopy (SEM) revealed that the Cu foil surface became cubic and had a smooth (100) surface after 100 cycles. By testing the electrocatalytic characterizations of Cu, among three kinds of Cu foil (polished Cu foil, 10-cycle Cu, and 100-cycle Cu), the 100-cycle Cu showed the highest C_2 Faradaic efficiency up to 60.25% and maintained the stability of C_2 production after 2.5 h chronoamperometric measurements. The high C_2 selectivity was attributed to the suppressed C_1 production due to the increased interfacial pH value and the improved C_{2+} activity caused by the stepped facets on (100) surface.[62] Moreover, pure metal catalysts loading Cu clusters on carbon materials, such as graphene, nanotube, and nanodiamond, introduce another development trend of Cu-based catalyst enhancement. Cu atoms of the interface between Cu clusters and carbon substrate were reported to be partially oxidized, which further endow Cu atoms with relatively strong adsorption energy.[63] Cui et al. sputtered Cu clusters on N-doped nanodiamond (N-ND) to form N-ND/Cu via microwave plasma CVD. In comparison to N-ND, the onset potential of N-ND/Cu exhibited a large positive shift, thereby suggesting that the additional Cu markedly reduced the reaction overpotential. The Cu atoms of the interface showed a large binding strength with *CO and further permitted C—C coupling due to the formal principle. C_2 eventually became the main reduction products, and unnecessary side reaction was efficiently suppressed. Therefore, a high C_2 Faradaic efficiency of 63% was observed, and the remarkable C_2 production rate reached nearly 90 µmol L^{-1} h^{-1}.[65] Similar to many other metal-based catalysts, the addition of organic molecules not only protects the Cu-based catalyst surface from corrosion but also changes the binding energy with different intermediates and contributes to the inhabitation of scaling relations,

as discussed in Section 2.2.1. Therefore, desired products are easily obtained for metal molecule complexes by only changing the position and types of ligands.[66] Sargent et al. discovered the CRR catalysis contributions of a type of N-aryl-substituted tetrahydro-bipyridine species 1–11 (**Figure 5**a) by depositing them on the Cu electrode. The entire test was performed in a liquid-electrolyte flow cell system, and Faradaic efficiency data were used to establish the volcano plot, which revealed the two crucial points. 1) The Bader charge of N atoms of N-aryl-substituted tetrahydro-bipyridine had a large ratio impact of absorbed atop- and bridge-bound CO (CO_{atop}/CO_{bridge}). 2) $CO_{atop} \cdot CO_{bridge}$ exhibited a close relationship with the final product, namely ethylene selectivity (Figure 5b,c). Moreover, the DFT calculation in Figure 5d displayed that the moderate co-existence of CO_{atop} and CO_{bridge} efficiently reduced the energy barrier of CO dimerization; thus, tuning the ratio of CO_{atop} to CO_{bridge} by changing the Bader charge of N atoms of nitrogenous ligands, such as cysteamine, thiols, and polypyrrole, is crucial.[64]

Types of innovative metal-based materials, namely oxide-derived metals, have been considered promising catalysts in the field of CRR catalysis. Kanan et al. first fabricated oxide-derived Cu (OD-Cu) and applied it to CRR. Cu foil was annealed in air during synthesis to form the Cu_2O layer, and Cu_2O was then reduced in high temperature. This unique synthesis can produce high-density grain boundaries containing numerous active sites.[67] Lum and Ager comprehensively investigated the selectivity of various active sites on OD-Cu via isotopic composition analysis. The analysis results revealed that three types of products, namely ethanol, ethylene, and 1-propanol, were generated on different active sites.[68] However, these results still failed to specify the relationship between products
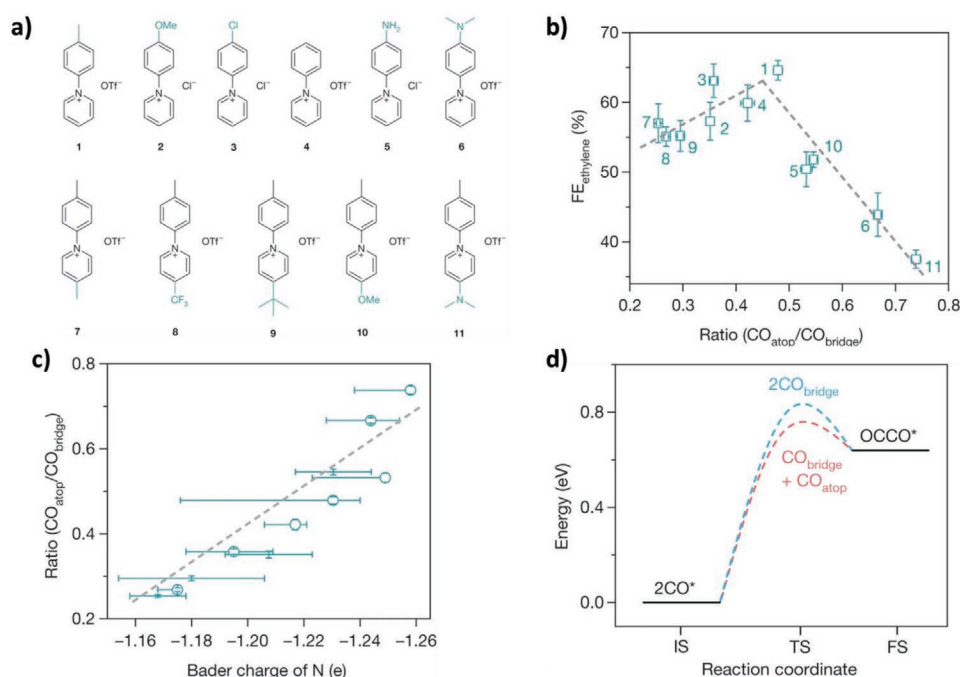

Figure 5. a) Molecular structures of additives 1–11. b) The relationship between the ethylene FE and the ratio of COatop/CObridge. c) The relationship between the ratio of atop CO to bridge CO and the Bader charge for the N atom. d) Energy barriers of the dimerization of two CO at both bridge sites and two CO at bridge and atop sites. Reproduced with permission.[64] Copyright 2020, Nature Publishing Group.

**ADVANCED
SCIENCE NEWS**

www.advancedsciencenews.com

NANO · MICRO

small

www.small-journal.com

and active sites. He et al. recently found the residual presence of Cu_2O in OD-Cu by in situ and ex situ tests. P orbitals of O atoms possessed large impacts on the stability of intermediate adsorption and favored the conversion of CO_2 into ethylene. Thus, researchers obtained a desirable method to manufacture optimal products with OD-Cu catalysts.[69]

Apart from C_2 products, C_3 products formation on Cu-based catalysts recently has breakthrough, by electroreducing CO_2 to n-propanol. Peng et al. synthesized CuS containing rich double sulfur vacancies, by utilizing lithium tuning method. The n-propanol Faradaic efficiency reached 15.4% and n-propanol partial current density was up to 9.9 mA cm^{-2}, both of which were the highest among all reports about n-propanol generation. From DFT result, it was suggested that this structure was able to stabilize $^*CO$ and $OCCO^*$ intermediates, and promoted the coupling of them to from *C3, which was key intermediate of n-propanol generation.[70]

2.2.3. Metal Oxides

Different from reaction pathways on pure metal catalysts, most CRR intermediates are likely to bind through their oxygen atoms and those of metal oxides. This condition suggests that metal oxides show more selectivity of oxygenates than pure metal catalysts.[71]

On the film surface, Co atoms with low coordination numbers are considered to be the main adsorption sites for CO_2 on Co ultrathin film.[72] Moreover, structure distortion on films decreases surface energy, resulting in stability enhancement. Hu et al. synthesized 1.72 nm thick ultrathin Co_3O_4 layers, which showed remarkable electrocatalytic properties for the reduction of CO_2 to formate. The Faradaic efficiency of these layers reached 64.3% at −0.88 V versus SCE, which was three times higher than bulk Co_3O_4. The current density of the layers also reached 0.68 mA cm^{-2}, which was 20 times higher than their bulk counterpart. The Tafel plots of formate revealed that Co atoms on film surface played a vital role in stabilizing the CO_2^- intermediate, which is consistent with the aforementioned theory.[73]

Cu^+ of Cu_xO catalysts prefers to adsorb intermediates, especially $^*CO$, during the CRR process, and substantially convert CO_2 into ethylene.[69] Furthermore, some defect sites of Cu_xO catalysts, such as oxygen vacancies, enhance the bond strength of $^*CO$ intermediate and ethylene selectivity.[75] Gu et al. reported that CuO_X nanocatalysts with a highly branched high density of oxygen vacancies (CuO_X-Vo) showed high activity and selectivity to convert CO_2 into ethylene. The ethylene Faradaic efficiency reached 63% at −1.4 V versus RHE. The partial current density of products remained unchanged in the first 13 h, and the Faradaic efficiency only slightly dropped after 12 h, thereby demonstrating the high stability of CuO_X-Vo. The DFT results showed that the oxygen vacancies promoted the adsorption of $^*CO$ and $^*COH$ intermediates and the low affinity to $^*CH_2$, which further reacted with another $^*CH_2$ intermediate and formed ethylene. This new catalyst effectively promoted the entire reaction process.[76] Unfortunately, the electric field reaction leads to the reduction in Cu^+ to Cu^0, which results in a large attenuation of ethylene selectivity.[77] Yu et al. designed a type of spherical Cu_2O nanoparticles with moderate nanocavities

(multi-hollow Cu_2O catalyst) to inhibit this harmful reduction. Compared with two other Cu-based catalysts, namely fragmental Cu_2O and solid Cu_2O catalysts, multi-hollow Cu_2O catalysts displayed increased C_{2+}/C_1 product selectivity of 8.5 and C_{2+} partial current densities reaching 267 mA cm^{-2} (**Figure 6**a,b, respectively). Furthermore, among all C_{2+} products, ethylene accounted for the largest proportion of 38%, which was more than the sum of the other C_{2+} products. Thus, C_{2+} Faradaic efficiency and total current density maintained their remarkable stability after 180 min test due to the aforementioned reasons (Figure 6c). From kinetics viewpoint, numerous intermediates were confined on the catalyst surface due to the structure of nanocavities. Gathered intermediates not only rendered additional chances for C—C coupling to form C_{2+} products but also inhibited Cu^+ reduction (Figure 6d).[74]

2.3. Organic Polymer

2.3.1. Metal–Organic Frameworks (MOFs)

With the development of reticular chemistry, MOFs, as one of the porous, crystalline, and extended materials, have become a popular research topic. Precise and molecular-level control is easily conducted for MOF synthesis through molecular and framework chemistry. Unsaturated metal sites play a vital role because they endow MOFs with remarkable CO_2 adsorption at low pressure. However, the competition of water molecules on the unsaturated metal sites reduces CO_2 uptake, which is an intractable challenge to deal with.[78] Hinogami et al. first applied MOFs as electrocatalysts to reduce CO_2. They synthesized copper rubeanate MOF (CR-MOF), and its major product was formic acid. CR-MOF exhibited 0.2 V more positive onset potential and a larger yield of formic acid compared with the Cu electrode. CR-MOF showed slightly weak CO_2 adsorption and led to the high selectivity of formic acid up to 98% due to the ionic metallic site and low density of CR-MOF. However, effectively controlling pore size must still be comprehensively explored.[79] Cu-MOF also showed considerable CO_2 capture capability and increased CO_2 concentration in aqueous solution. The entire electrode displays marked improvement of methane Faradaic efficiency from 2.5% to 20% at −1.8 V versus SCE compared with blank gas diffusion electrode (GDE) with the introduction of Cu-MOF into GDE). However, the weight ratio of Cu-MOF would effectively be controlled under 10% because additional Cu-MOF decreased GDE active sites and provided extra carbon sources for HER.[80]

Although MOF possesses numerous merits, this framework also has defects in poor electron-donating capability and electrical conductivity. Herein, in addition to the metal center, ligand doping also plays a key role in CRR catalysis. The synergetic effect of ligand and C atoms on MOF is crucial to the enhancement of MOF catalytic capacity, especially when the metal center is not an ideal electron donor. Dou et al. reported that 1,10-phenanthroline-doped Zn-based MOFs of zeolitic imidazolate framework-8 (ZIF-8) possessed high CO Faradaic efficiency of up to 91%. DFT calculations showed that charge transferred from introduced phenanthroline molecule to the adjacent sp^2 carbon atom sites in imidazolate. Sp^2 carbon atom
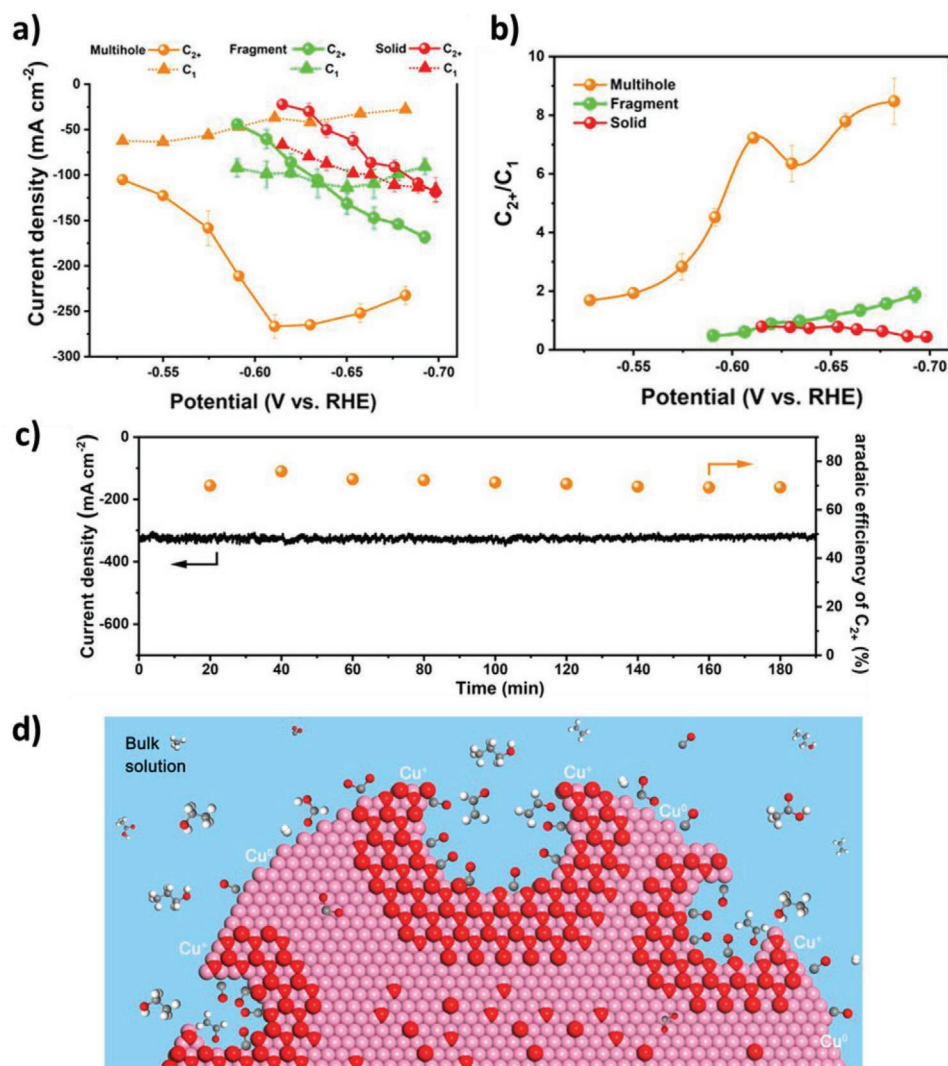
ADVANCED
SCIENCE NEWS
www.advancedsciencenews.com

NANO · MICRO
small
www.small-journal.com

Figure 6. a) C2+ and C1 partial current densities and b) C2+/C1 product selectivity at different applied potentials. c) Stability test for 3 h of CO2 electrolysis. d) Schematic of carbon intermediates confined in the nanocavities. Reproduced with permission.[74] Copyright 2020, American Chemical Society.

sides became the main electrocatalytic active sites, which promoted electron movement to CO_2 orbit and facilitated vital *COOH immediate formation.[82] Wang et al. used reductive polyoxometalates (POMs) and metalloporphyrins to form polyoxometalate–metalloporphyrin organic framework (PMOF). Among all PMOFs, Co-PMOF had a prominent capability to convert CO_2 into CO with the highest Faradaic efficiency of 99% at −0.8V versus Ag/AgCl (**Figure 7**a) and TOF of 1656 h^{-1} (Figure 7b). The coordination effect of reductive POM and Co-porphyrin enhanced the electron-rich unit and electron mobility of Co-PMOF. *COOH and *CO were quickly formed due to high electron conductivity of Co-PMOF and POM, as an electron-rich unit, facilitated CO_2 desorption (Figure 7c,d).[81]

2.3.2. Covalent Organic Frameworks

The building blocks of COF are arranged systematically because of its predesignable crystalline framework structure, and desired physicochemical feature is generated.[84] Molecularly defined pores (**Figure 8**a) endow COF with maximum CO_2 uptake capability, which reaches 1200 mg g^{-1} for COF-102 at 55 bar and 298 K.[79b,85] However, low stability is still a major problem in COF practical application due to its unidirectional crystallization.[86]

Liu et al. reported that highly crystalline amine COF with amine linkage showed excellent CO conversion efficiency. Discrete frontier orbitals of amino functional groups combined with CO_2 in specific orientations and enhanced CO selectivity. The entire electrode displayed high CO Faradaic efficiency of 80% at −0.85 V versus RHE when loaded on an Ag electrode surface (Figure 8b,c). Moreover, the amine linkage facilitated COF stability in strong acids and bases.[83] Lin et al. prepared COF-366-Co and COF-367-Co via imine-condensation of 5,10,15,20-tetrakis (4-aminophenyl) porphinato cobalt and 1,4-benzenedicarboxaldehyde or 4,40-biphenyldicarbaldehyde. The catalyst also had remarkable activity and selectivity to CO products with high Faradaic efficiency of 90% and initial TOF of up to 9400 h^{-1}.[87]

**ADVANCED
SCIENCE NEWS**

www.advancedsciencenews.com

NANO · MICRO
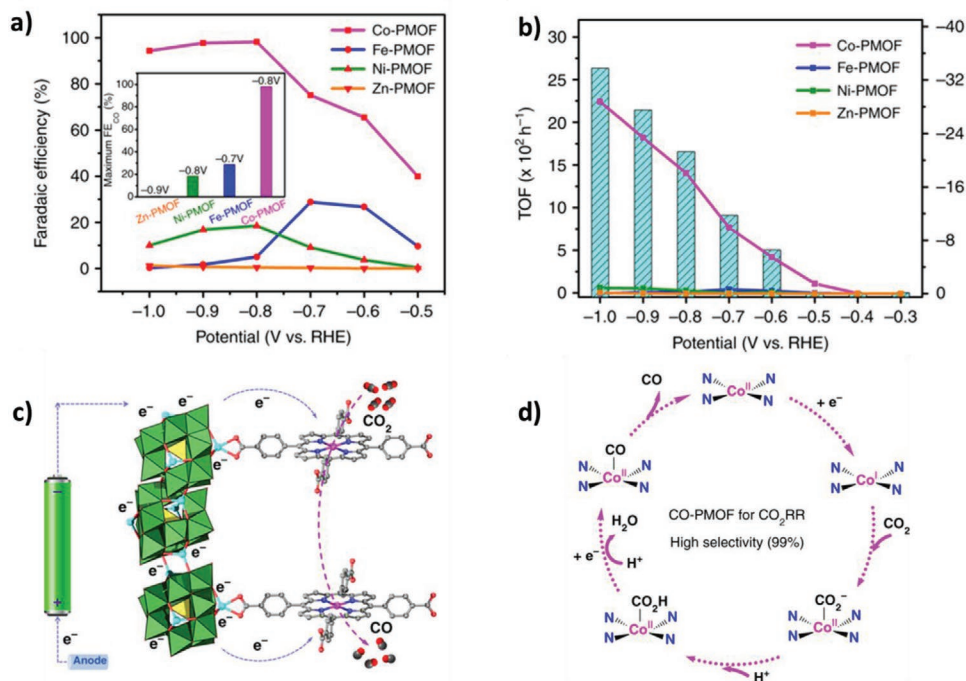**small**
www.small-journal.com

Figure 7. a) Faradaic efficiencies for CO, b) partial CO current density, and c) TOFs. d) Proposed mechanistic scheme for the CRR on Co-PMOF. Reproduced with permission.[81] Copyright 2018, Nature Publishing Group.

2.4. Carbon-Based Materials

Nitrogen-doping graphene is one of the most common materials used to enhance the CRR catalytic capability of graphemes. Among different N defects, pyridinic-N sites exhibit strong CO_2 adsorption and the lowest energy barrier of *COOH immediate formation because N defects process high affinity with *COOH.[12b,88] Major reduction products of N-doped graphene are usually CO, formic acid, and methane.[89] Defected graphene is also reported to be a potential candidate for CRR catalysts. The DFT calculation results
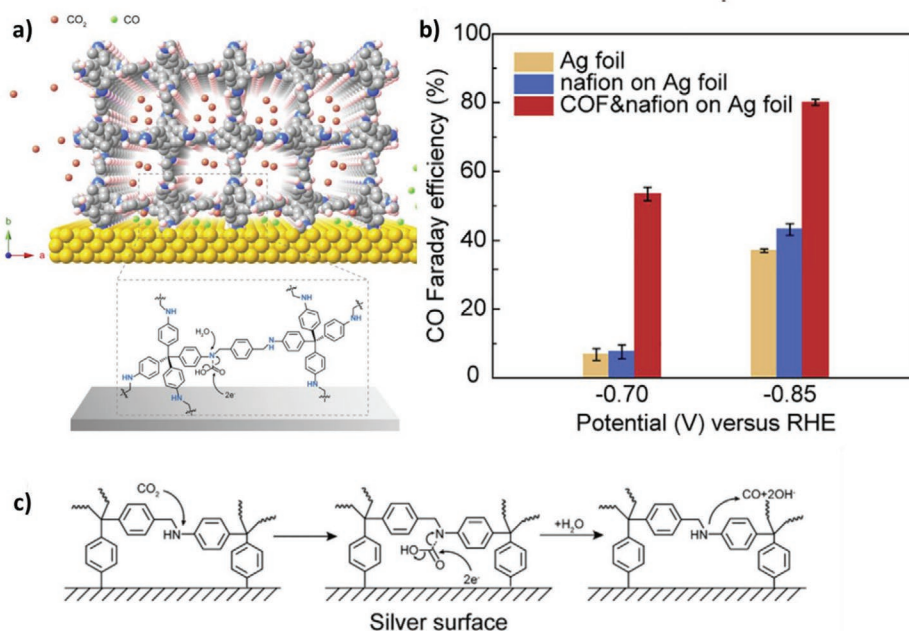

Figure 8. a) Illustration of the molecularly defined interface. b) Faradic efficiency for CO. c) Mechanism scheme of concerted CO_2 reduction at the interface between COFs and the silver electrode. Reproduced with permission.[83] Copyright 2018, Elsevier.

revealed that electron localization in the defected sites of graphene has low bond energy with CO, indicating that its main reduction product is CO. Furthermore, defected graphene has more CRR selectivity than HRR, but its catalytic capability is not as effective as N-doped graphene.[90] Han et al. used experiment results to prove this theory. They synthesized defective graphene (DG) with a nitrogen removal method. DG had remarkable CO_2 chemisorption capability and high CO Faradaic efficiency of 84% at −0.6 V versus RHE. This study successfully proved the theoretical calculation and may lay the foundation of the DG application.[91]

Similar to graphene, nitrogen doping is also an ideal method to enhance the CRR catalytic capability of CNT and strengthen the selectivity for CO generation with considerably low overpotential than pristine CNT. Furthermore, the morphology of CNT is transformed to bamboo-shape (**Figure 9**a) with the introduction of pyridinic-N, thus showing high CO Faradaic efficiency over 80% (Figure 9b) and substantially positive onset potential (Figure 9c).[92] The DFT results revealed that pyridinic-N on CNT exhibited appropriate binding energy with *COOH immediate, showing a low energy barrier of the potential-limiting
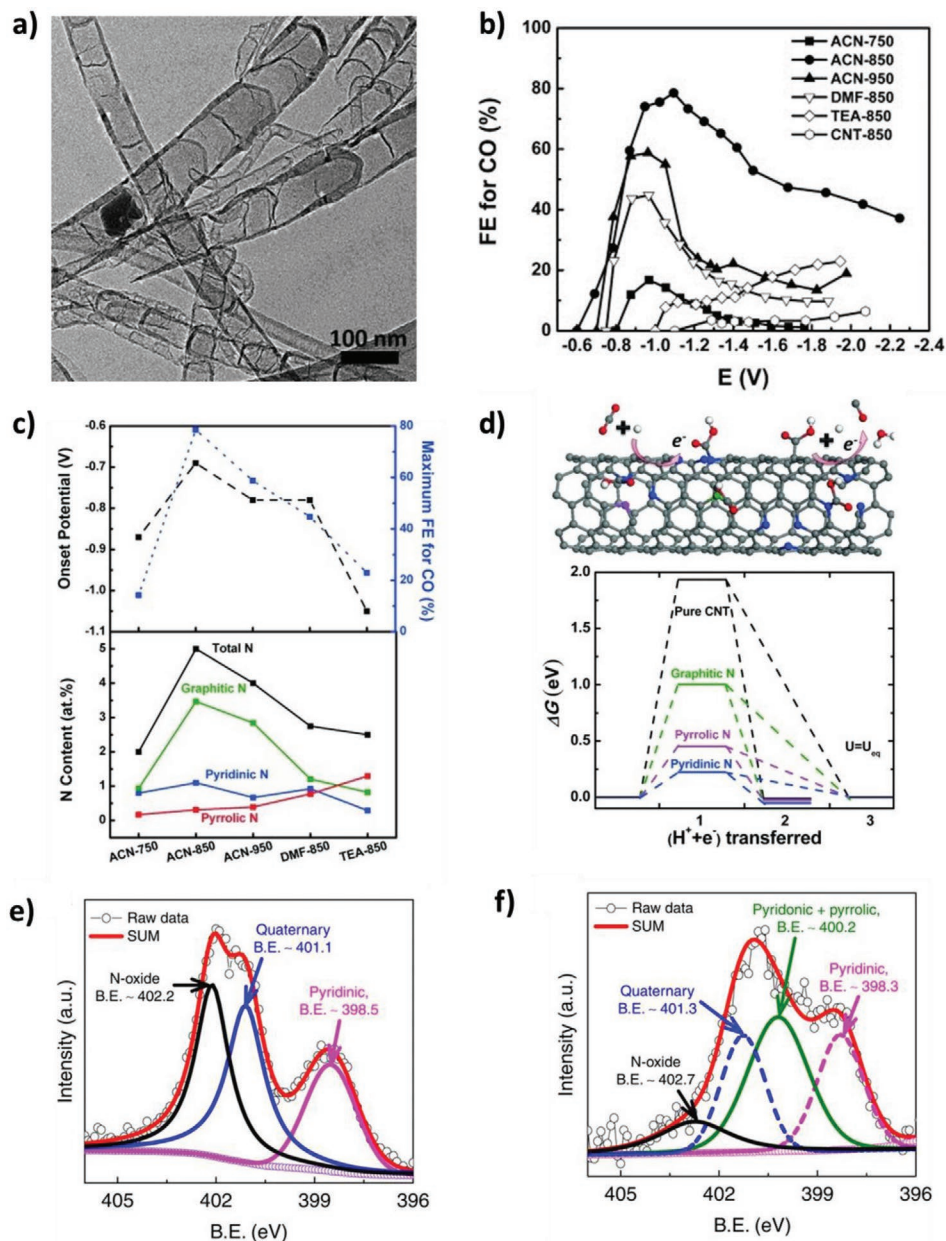

Figure 9. a) TEM image of NCNTs. b) Faradaic efficiency for CO versus potential on NCNTs synthesized using different precursors and growth temperatures. c) The onset potential and maximum Faradaic efficiency for CO formation as a function of N content in the synthesized NCNTs. d) Schematic illustration of CO formation on the NCNTs and free-energy diagram at equilibrium potential for CRR. Reproduced with permission.[92] Copyright 2015, Wiley-VCH. Deconvoluted N1s spectra for CNFs before e) and after f) the experiment. Reproduced with permission.[93] Copyright 2018, Nature Publishing Group.

**ADVANCED
SCIENCE NEWS**

www.advancedsciencenews.com

**NANO · MICRO
small**

www.small-journal.com

step (Figure 9d).[94] In addition to the N atom, other additives, such as complex or other carbon materials, result in an interesting phenomenon. Guo et al. manufactured distinguished hybrid catalysts containing ZIF and MWCNT, which exhibited tremendous CO Faradaic efficiency up to nearly 100% at −0.86 V versus RHE at a high current density of 7.7 mA cm^{-2}. The XPS analysis result showed that the synergetic effect of a considerable amount of pyridinic N and the efficient transport of electron and mass, as the unique feature of CNT, contributed to the remarkable catalytic capability.[95] CNT is considered to be an ideal candidate for the catalysts of CO_2 battery because of its remarkable CO_2 adsorption of CNT. Hu et al. took a-MCNT as a cathode catalyst on Na-CO_2 battery. a-MCNT was proven to improve the speed of Na$^+$ dendrite-free plating/stripping and adsorb CO_2 efficiently.[13]

Carbon nanohorn (CNH), especially oxidized CNH, possesses open nanowindows, which endow excellent CNH adsorption. CNHs ordinarily form dahlia-like aggregates, which provide CNH with three types of adsorption sites: CNH tips, CNH sidewalls, and the central empty cavities within the dahlias.[96] However, the CRR catalytic capability of CNH is not ideal because of the weak bond between CO_2 and carbon surface. Melchionna et al. integrated Pd@TiO_2 nanoparticles on ox-SWCNH. This integration showed a high formic acid yield with high Faradaic efficiency of nearly 99% at −0.13 V versus RHE in the first 5 min of electrolysis. By contrast, HRR gradually became the dominant reaction as the reaction continued.[97] Liang et al. loaded N-doped single-wall CNH (N-SWCNH) on the cathode of the Na-CO_2 battery. Compared with CNT, Raman results demonstrated that N-SWCNH had large defect sites and disorder degrees, indicating that N-SWCNH contained additional active sites to facilitate contact with CO_2 and conduct catalysis. Until now, among all Na-CO_2 batteries, this battery displayed the lowest discharge–charge overpotential of 0.61 V at the current density of 0.1 mA cm^{-2}.[98]

Carbon nanofiber (CNF) is an ideal candidate for catalyzing CRR with two electrochemically active species: 1) pyridinic-N and 2) positively charged carbon atoms. Kumar et al. reported that polyacrylonitrile-based heteroatomic CNF had a remarkable capability to reduce CO_2 to CO at negligible overpotential (0.17 V), high Faradaic efficiency of 98% at −0.573 V versus SHE, and current density of up to 15 mA cm^{-2}. The XPS analysis showed that during the reaction, content of N-oxide and pyridinic nitrogen, which was traditionally considered as active sites, decreased but the catalytic performance was unchanged (Figure 9e,f). Therefore, compared with nitrogen elements, oxidized carbon atoms play a vital role in CRR by forming strong bonds with CO_2 intermediate complex because of its high atomic charge and spin density.[93] Fang et al. developed nanowire-decorated carbon fibers (CMO@CF) and applied them in the Na–CO_2 battery. The discharge product Na_2CO_3 was easily decomposed due to its porous homogeneous morphology, and this specific structure rendered batteries with low overpotential and high stability.[99]

Carbon black has considerable electron conductivity and highly irregular hydrophobic surface of mesoporous.[100] Moreover, carbon black has promising applications in solar energy, fuel cells, and lithium-ion batteries. In recent years, carbon black played an important role in the electrodes and substrates

of catalysts in the field of metal–CO_2 battery. Xu et al. applied super P carbon black on the cathode of Li–CO_2 battery and remained stable even at high temperatures of 100 °C.[101] The application of Ketjen black as a cathode catalyst on Li–CO_2 battery was also reported. The rechargeability of the Li–CO_2 battery was possible via Ketjen black.[102]

Apart from nitrogen-doped carbon material, sulfur and phosphorus are attractive doped candidates. Liu et al. first introduced phosphorus-doped carbon material as CRR electrocatalysts, by synthesizing phosphorus doped onion-like carbon (P-OLC). The P−C bonds of P-OLC exhibited strong electron transfer capability and binding energy of key intermediate *COOH. These superior characteristics rendered catalysts with high CO Faradaic efficiency of 81%.[103] Furthermore, the addition of phosphorus and sulfur to form co-doped with nitrogen is reported to enhance selectivity and activity of pyridinic and graphitic N, and it can further decrease energy barrier of *COOH immediate formation.[104] Han et al. recently made some breakthroughs on nitrogen and phosphorus co-doped carbon aerogels (NPCA) to acquire excellent catalysts for the reduction of CO_2 to CO. The electrochemical measurement exhibited that NPCA had maximum CO Faradaic efficiency of 99.1% at −2.4 V versus Ag/Ag$^+$. Partial current density reached −143.6 mA cm^{-2} at the same potential, which was the highest current density to date.[105]

Last but not least, metal impurities, involving Fe, Ni, Co, Mo, Mn, V, and Cr, may appear in carbon-based catalysts, due to deposition of metal ions from electrolyte and residue of metal catalysts during the synthesis process. They are hardly to be removed thoroughly and small amount of them can display great impact on the whole catalytic process.[106] The effect of metal impurities is under heat debate and many researches have been taken to trace it.[107] Lum et al. took research on CRR catalytic performance of graphene oxide with different concentrations of Cu impurity (Cu(X)GO). It showed that only 120 ppm Cu content endowed Cu(X)GO with 54.67 mmol g^{-1} s^{-1} methane mass activity. Moreover, Cu(X)GO exhibited four to five times higher activity than pure Cu particles.[108] Furthermore, metal impurities are able to interact with other doped elements to enhance catalytic ability. Kim et al. reported that Fe impurities from electrolyte interacted with N sides of nitrogen-doped carbon well, with the aid of self-activation. The Fe–N interaction displayed brilliant stability, which kept 90% CO Faradaic efficiency and more than 3.8 mA cm^{-2} current density after 120 h operation.[109]

Overall, **Figure 10** shows the performance comparison of four types of electrocatalysts considering the activity, selectivity, price, stability, and electron conductivity. Moreover, this review provides a clear cognition of the selection of suitable CRR catalysts in the future by comparing their catalytic capability.

3. Metal–CO_2 Batteries

CO_2 coupling on battery is an attractive way to mitigate energy and environmental crisis. The application of CO_2 on batteries was firstly observed by adding CO_2 in supply gas of Li–O_2 batteries. Until now, this field has attracted more and more attention, based on the following merits. 1) metal–CO_2 batteries are
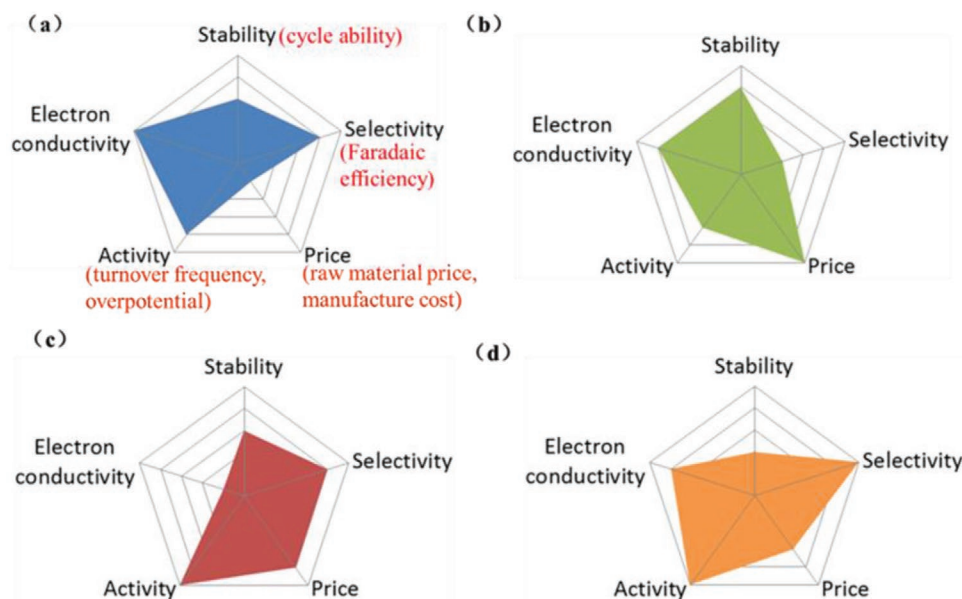
Figure 10. Road maps of the performance properties of different types of electrocatalysts: a) noble metal and relative compounds, b) transition metal and relative compounds, c) organic polymer, and d) carbon-based metal-free materials.

able to consume greenhouse gas CO_2 and generate electricity, playing the role of killing two birds with one stone; 2) owing to great diffusion of intermediate like peroxydicarbonate ion, final products of CO_2 reduction are more likely to fill void volume of electrodes. Herein, metal–CO_2 batteries exhibit large capacity and discharge voltage; 3) discharge products, like carbon and formate, possess high energy density and economic value.[110] Depending on the difference in energy conversion, metal-CO_2 batteries are divided into two parts: Li/Na-CO_2 and Zn/Al-CO_2 systems. Li/Na-CO_2 system exhibits more substantial energy density than that of the Zn/Al-CO_2 system and is a promising electricity supply. However, Zn/Al-CO_2 systems display extraordinary selectivity to convert CO_2 into valuable carbonaceous products.[111] The electrochemical properties of four types of metal–CO_2 batteries are listed in **Table 2**. However, there are several problems, inhibiting the progress of metal–CO_2 batteries. 1) discharge reaction requires large overpotential, which is likely to decrease battery energy efficiency; 2) unstable anode metals and flammable electrolyte bring many security risks to batteries; 3) reduction products carbonate is low electron conductivity and difficult to decompose.[112] In order to tackle these challenges, it is necessary to take research on three aspects: 1) employing bifunctional electrocatalyst which is active for oxidation and reduction; 2) improvement of battery structure by applying solid electrolyte and liquid anode to enhance ion conductivity and operational stability of batteries; 3) tuning cathode electrolyte composition to convert discharge products into carbonaceous products with high electron conductivity.

3.1. Li–CO_2 Batteries

Li–CO_2 batteries possess higher energy and power densities compared with state-of-the-art Li-ion batteries.[124] However, the decomposition of Li_2CO_3, which is one of the major

discharging products, is difficult during the charge process. Furthermore, Li_2CO_3 is an electrical insulator and may cause harmful impacts on the electron transport of the cathode–electrolyte interface. Herein, high discharge–charge overpotential and poor cyclability are urgent defects on Li–CO_2 batteries. Xu et al. tested primary Li–CO_2 batteries in high temperatures. The capacity of Li–CO_2 batteries reached 2500 mAh g^{-1} at a current density of 0.05 mA cm^{-2} with a temperature of 80°C when super P carbon black was used as a cathode. By comparing the equilibrium potential with the actual discharge potential, $2Li + 2CO_2 \leftrightarrow Li_2CO_3 + CO$ initially dominated, but the actual discharge potential then reached the region of reaction $4Li + 3CO_2 \leftrightarrow 2Li_2CO_3 + C$ at high temperatures.[101]

Rechargeable batteries show better traits than primary batteries. The first rechargeable Li–CO_2 battery was reported in 2014. Ketjen black was taken as a cathodic catalyst and cycled in a mixture of $LiCF_3SO_3$ and TEGDME (1:4 in mole). The discharge capacity of Ketjen black was as low as 1000 mAh g^{-1}, which was only half of that of the primary Li–CO_2 battery. Moreover, this battery showed large discharge–charge overpotential and low round trip efficiency due to the accumulation of poor conductive Li_2CO_3, indicating that further comprehensive optimization should be conducted.[102] Therefore, promoting the decomposition of discharging products plays a key role in enhancing the cycling capability of batteries. Qiao et al. took Ru as a cathode, which had a remarkable capability to co-discompose discharging products of carbon and Li_2CO_3. Compared with solo decomposition, co-composition was not limited by thermodynamic equilibrium potential (3.82 V vs Li/Li$^+$) and introduced low overpotential.[113] Jin et al. employed carbon quantum dots (CQDs) supported by holey graphene (hG) (CQD/hG-0.3 hG = 0.3 wt/wt) as a cathodic catalyst in Li-CO_2 batteries. The catalyst exhibited a low overpotential of 1.02 V (vs Li/Li$^+$) at a current density of 0.1 A g^{-1} and a large discharge

Table 2. Comparison of electrochemical performances of different metal-CO_2 batteries.

Battery	Cathode	Electrolyte	Applied current	Discharge capacity	Voltage gap	Cycle ability	Refs.
Li–CO_2	Super P	1 M LiTFSI	0.05 mA cm^{-2}	2500 mAh g^{-1}	–	–	[101]
	KB	LiCF$_3$SO$_3$	30 mA g^{-1}	1000 mAh g^{-1}	1.6 V	7 cycles	[102]
	Ru	LiClO$_4$–DMSO	5 μA	10 μAh	1.3 V	–	[113]
	Au	LiClO$_4$–DMSO	5 μA	10 μAh	1.5 V	20 cycles	[113]
	Au	LiClO$_4$–DMSO	20 μA	20 μAh	2.2 V	–	[113]
	CQD/hG	LiTFSI	0.5 A g^{-1}	12 300 mAh g^{-1}	1.02 V	235 cycles	[114]
	Cu-NG	–	0.2 A g^{-1}	1000 mAh g^{-1}	0.77 V	50 cycles	[115]
	Ru-Cu-G	–	0.2 A g^{-1}	1000 mAh g^{-1}	0.88 V	100 cycles	[116]
	CPE@CNT	LiTFSI	50 mA g^{-1}	9000 mAh g^{-1}	1.4 V	50 cycles	[117]
Na–CO_2	CMO@CNF	NaClO$_4$	0.1 mA cm^{-2}	500 mAh g^{-1}	1.95 V	75 cycles	[99]
	a-MCNT	PVDF-HF-4% SiO$_2$/NaClO$_4$	0.5 A g^{-1}	1000 mAh g^{-1}	1.5 V	400 cycles	[13]
	MCNT	Poly/NaClO$_4$/SiO$_2$	50 mA g^{-1}	1000 mAh g^{-1}	0.6 V	240 cycles	[118]
	Nanohorn	Na$_3$Zr$_2$Si$_2$PO$_{12}$	0.1 mA cm^{-2}	2293 mAh g^{-1}	0.61 V	300 cycles	[98]
	Nanocarbon	polymer	300 mA g^{-1}	10 500 mAh g^{-1}	1.5 V	100 cycles	[119]
Al–CO_2	Carbon	EMIm]Cl/ AlCl$_3$	70 mA g^{-1}	13 000 mAh g^{-1}	–	50 cycles	[120]
	NPG@Pd	Ionic liquid	333 mA g^{-1}	2978 mAh g^{-1}	0.091 V	30 cycles	[121]
Zn–CO_2	NiPG	KHCO$_3$	0.5 mA cm^{-2}	–	2.4 V	60 cycles	[122]
	Porous Pd	NaCl	0.1 mA cm^{-2}	–	0.16 V	100 cycles	[23]
	CHF	[EMIM][BF$_4$]	0.4 mA cm^{-2}	340 mAh g^{-1}	–	–	[123]

capacity of 12300 mAh g^{-1} with a current density of 0.5 A g^{-1}. Moreover, the overpotential of this catalyst remained stable without large extensions after 235 cycles. The SEM image of CQD/hG-0.3 cathodic electrode showed that Li$_2$CO$_3$ overflowed in the electrode after the discharge process. Meanwhile, Li$_2$CO$_3$ was removed completely at the end of the recharge process. The coordinated effects between the structural framework provided by hG and high conductive CQD were proven to be crucial for the efficient formation and decomposition of Li$_2$CO$_3$.[114]

The aforementioned work indicated that Li$_2$CO$_3$ generates superoxide radicals, which may oxidize electrode and destroy battery stability.[116] Zhang et al. dispersed Cu nanoparticles on N-doped graphene acting as an efficient cathode. These nanoparticles showed a low discharge–charge overpotential of 0.77 V in the first cycle and remained stable after 50 cycles. The TEM and SEM images revealed the formation of approximately 3–5 nm thick CuO film on the Cu surface, which further protected the cathode from superoxide radical erosion.[115] Zhang et al. further integrated Ru-Cu nanoparticles co-depressed on graphene (Ru-Cu-G). CO_2 was absorbed around Cu and Ru particles homogeneously during the discharge process to form ultra-small discharge products evenly due to the interaction between Ru and Cu. Therefore, the rechargeability of the battery was considerably enhanced. Moreover, the XPS analysis results showed that the electron cloud density was changed by the coordinated effects of two metals and then affected the reciprocal electron binding energy. This unique property withstood nucleophilic attacks and decreased the existence time of superoxide radicals, leading to remarkable cycle performance. The results showed the low discharge–charge overpotential of 0.88 V after 100 cycles at a current density

of 200 mA g^{-1} and maintained high Coulombic efficiency of 67.9%, which demonstrated superior performance to Cu-G (58.1%) and Ru-G (60.7%).[125]

In addition to catalysts, liquid-free electrolytes are also crucial in Li–CO_2 batteries because of the leakage risk. Hu et al. reported a flexible quasi-solid-state battery with PMA/PEG-LiClO$_4$-3 wt%SiO$_2$ (CPE) as electrode and CNT as cathode materials. The warping cross-stacked CNT on CPE formed integrated cathode (CPE@CNT). This subtle design endowed the battery with reduced interface resistance and excellent electrochemical stability. The battery showed a low discharge–charge overpotential of 0.7 V even after 100 cycles and a large reversible energy density of 521 Wh kg^{-1}.[117]

Different from general discharge reactions, obtaining different Li–CO_2 discharge products via tuning catholytes and catalysts is possible. The most observed product is Li$_2$C$_2$O$_4$, which is a common intermediate of discharge reaction and easily decomposed.[113] Wang et al. and Chen et al. observed the existence of Li$_2$C$_2$O$_4$ in the final products when Mo$_2$C/CNT was used as a cathode of Li–CO_2 battery (**Figure 11**a). Moreover, Wang simulated the charge density difference of Li$_2$C$_2$O$_4$ on the cathode surface, thereby verifying the stability of Li$_2$C$_2$O$_4$ (Figure 11b).[126,128] Wang et al. recently further simulated the generation mechanism of Li$_2$C$_2$O$_4$ on three Mo$_2$C facets, namely α-Mo$_2$C (001), β-Mo$_2$C (001), and β-Mo$_2$C (101), through DFT calculation and Bader charge analysis. The DFT results noted that all three facets exhibited less overpotential of Li$_2$C$_2$O$_4$ nucleation than Li$_2$CO$_3$ nucleation, indicating that Li$_2$C$_2$O$_4$ is likely to be the final discharge product on Mo$_2$C cathode catalyst. Moreover, energy profiles demonstrated that the splitting reaction of Li$_2$C$_2$O$_4$ into Li$_2$CO$_3$ should adsorb large amounts

ADVANCED
SCIENCE NEWS
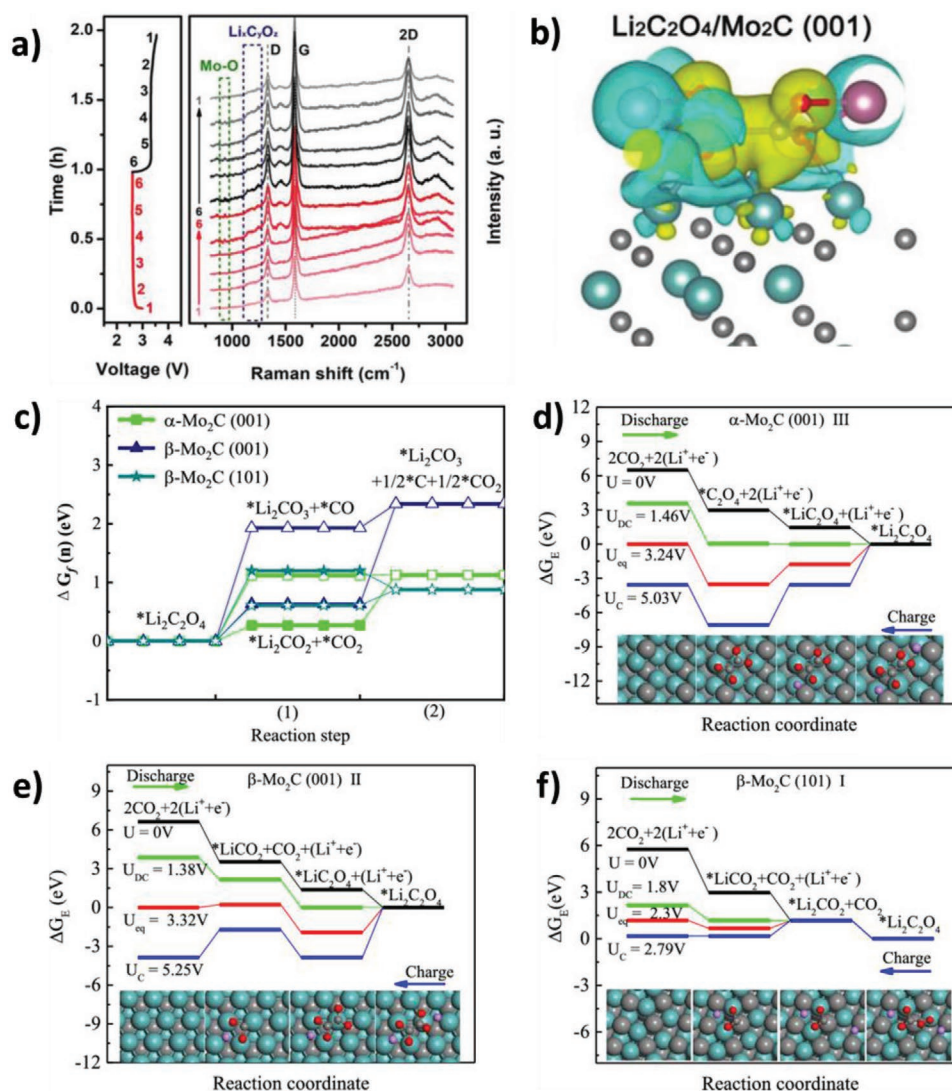www.advancedsciencenews.com

NANO · MICRO
small
www.small-journal.com

Figure 11. a) In situ Raman spectra of Mo_2C/CNT at 12 selected states during cycling with corresponding discharge/charge profiles on the left. b) Charge density difference of $Li_2C_2O_4$ adsorbed on Mo_2C. Reproduced with permission.[126] Copyright 2018, Wiley-VCH. c) Calculated energetic profiles for $Li_2C_2O_4$ splitting into Li_2CO_3 on three Mo_2C surfaces; electrochemical free-energy changes of Li-CO_2 batteries under different potentials with three d) Mo_2C:α-Mo_2C (001), e) β-Mo_2C (001), and f) β-Mo_2C (101). Reproduced with permission.[127] Copyright 2020, American Chemical Society.

of heat, thus offering strong support on the high stability of $Li_2C_2O_4$ on three facets (Figure 11c). Electrochemistry free energy plots revealed that β-Mo_2C (101) surface displayed the lowest overpotential on the generation of $Li_2C_2O_4$ (Figure 11d-f). Herein, increasing the β-Mo_2C (101) surface enhanced the $Li_2C_2O_4$ selectivity of Mo_2C.[127] In addition to the replacement of Li_2CO_3 with $Li_2C_2O_4$, on the Li–CO_2 system, converting CO_2 into formic acid, which is more valued than amorphous carbon, was initially achieved by Wang et al. The novel battery took $Li_{1.5}Al_{0.5}Ge_{1.5}P_3O_{12}$ as a solid electrolyte, NaCl solution as catholyte, and three-dimensional integrated Pd (3DI-Pd). Electrochemical measurements showed that 3DI-Pd catalyst possessed remarkable formic acid Faradaic efficiency of 61% and a substantial oxidation capacity of formic acid. The possible total battery reaction was $CO_2 + 2Li + 2H^+ \leftrightharpoons HCOOH + 2Li^+$ with the application of 3DI-Pd on Li–CO_2 due to these excellent traits. The entire battery system revealed high conversion efficiency of

CO_2 to formic acid due to the excellent traits of 3DI-Pd, thereby reaching 97% and maintaining a stable voltage gap after 10 h of testing at 2.78 mA cm^{-2}.[129] Therefore, this discovery breaks through current knowledge of CO_2 battery systems, laying the foundation of battery design with high energy density and valued discharge product formation.

3.2. Na–CO_2 Batteries

Na has a more massive reserve on the earth than Li. Compared with Li–CO_2 batteries, Na–CO_2 batteries exhibit a high energy density of 1.13 kWh kg^{-1}.[130] The total reaction of the battery is $4Na + 3CO_2 \leftrightarrow 2Na_2CO_3 + C$ ($E^{\ominus} = 2.35$ V).[13] However, some difficulties, such as poor cyclability and large overpotential, still hinder its development. Thus, developing carbon-based cathode materials with excellent surface and interface

ADVANCED
SCIENCE NEWS
www.advancedsciencenews.com

NANO · MICRO
small
www.small-journal.com

traits is an ideal strategy. Fang et al. synthesized the Co_2MnO_x nanowire-decorated carbon fibers (CMO@CF) to promote Na_2CO_3 decomposition. These carbon fibers manifested a low discharge–charge overpotential of 1.95 V at the current density of 0.1 mA cm^{-2} and remained stable over 75 cycles due to the porous homogeneous morphology of CMO@CF.[99]
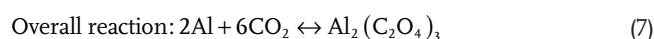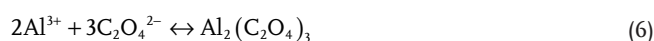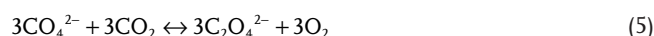
Another major challenge hampering the application of Na–CO_2 battery is security risks considering the leakage of combustible electrolytes and the instability of Na anode. Thus, constructing a type of all-solid-state battery is feasible. Wang et al. designed all-solid-state flexible Na–CO_2 batteries, which include Na anode, poly/NaClO$_4$/SiO$_2$ electrolyte, and MCNT cathode. These batteries showed high safety and distinguished cyclability of 240 cycles due to solid-state electrodes and dendrite-free Na anodes. Another unique feature is the prominent bendability of these batteries. The OCV and charge-transfer resistance (R_{ct}) of these batteries remained stable and continued to run for more than 80 h at different bending states (0 to 360°).[118] Li et al. recently designed an all-solid-state Na–CO_2 battery comprising Na anode, liquid-free polymer electrode, and N-doped nanocarbon cathode. The battery maintained stable overpotential after 100 cycles (400 h) of testing and electrolyte evaporation was disregarded. The DFT results showed that the presence of pyridinic N enhanced binding affinity with CO_2 and electron transfer. This brilliant merit rendered the entire battery system with remarkable discharge capacity exceeding 10000 mAh g^{-1} and an energy density of 180 Wh kg^{-1}. Moreover, the porous structure of cathodes helped CO_2 transfer freely and reduced interface resistance to some extent. Unfortunately, the all-solid-state Na–CO_2 battery exhibited a relatively large overpotential of more than 1 V compared with other Na–CO_2 batteries, indicating that the manufacture of perfect all-solid-state Na–CO_2 batteries should still be improved.[119]

In most of the aforementioned research, organic solutions, such as TEGDME, EC/DMC, and CPE, are adopted as electrolytes, which are normally flammable, poisonous, and poorly conductive. Liang et al. first applied the NaCl aqueous solution as catholyte on hybrid Na–CO_2 batteries and explored their electrochemical performance and reaction mechanism. In the current research, N-SWCNH was loaded on carbon paper to fabric cathode, and the NASICON structure solid electrolyte acted as the separator and combined with Na anode to form the hybrid Na–CO_2 battery (**Figure 12**a). Among all Na–CO_2 batteries, this type of battery exhibited the lowest discharge–charge overpotential of 0.61 V at a current density of 0.1 mA cm^{-2} (Figure 12b). Furthermore, this battery maintained stable discharge and charge plateau after 300 cycles (Figure 12c) and showed a high capacity of 2293 mAh g^{-1} (Figure 12d). The result of in situ Raman and ex-suit XRD indicated that CO_2 was reduced to C and Na_2CO_3, and Na_2CO_3 further reacted with H_2O to form $NaHCO_3$ (Figure 12e,f).[98]

3.3. Al–CO_2 Batteries

The content of Al ranks third in the earth's crust. Compared with Li and Na, Al has superior merits on high safety, low cost, and high energy density of 2980 Ah kg^{-1}.[131] Archer et al. took O_2 as a type of auxiliary gas to integrate Al–CO_2 battery

(Al/CO_2-O_2) and used 1-ethyl-3-methylimidazolium chloride ([EMIm]Cl)/aluminum chloride (AlCl$_3$) as electrolytes. The results of DART-MS, SEM-EDXS, XPS, and TGA-FTIR revealed that the major discharge product was $Al_2(C_2O_4)_3$. Based on the reaction model of Li/CO_2-O_2 and Na/CO_2-O_2 battery, the following reaction mechanisms of Al/CO_2–O_2 batteries were assumed.

$$2Al \leftrightarrow 2Al^{3+} + 6e^- \tag{1}$$

$$6O_2 + 6e^- \leftrightarrow 6O_2^- \tag{2}$$

$$3CO_2 + 3O_2^- \leftrightarrow 3CO_4^- \tag{3}$$

$$3CO_4^- + 3O_2^- \leftrightarrow 3CO_4^{2-} + 3O_2 \tag{4}$$

$$3CO_4^{2-} + 3CO_2 \leftrightarrow 3C_2O_4^{2-} + 3O_2 \tag{5}$$

$$2Al^{3+} + 3C_2O_4^{2-} \leftrightarrow Al_2(C_2O_4)_3 \tag{6}$$

$$\text{Overall reaction: } 2Al + 6CO_2 \leftrightarrow Al_2(C_2O_4)_3 \tag{7}$$

This type of battery could also show promising industry applications. The content of CO_2 reached 80% in a flue gas stream. A total of 4.89 kg CO_2 kg^{-1} Al was captured and used to generate electric power. This battery reduced 1.97 kg CO_2 kg^{-1} Al based on the energy density of 3.58 kWh kg^{-1} Al and CO_2 emissions of 0.55 kg CO_2 kWh^{-1}. The main discharge product $Al_2(C_2O_4)_3$ was decomposed to $H_2C_2O_4$ and Al_2O_3, indicating the remarkable improvement of the economic benefit (**Figure 13**). This improvement further demonstrated that the reuse of Al_2O_3 on aluminum smelting resulted in large economic values.[120] Ma et al. reported rechargeable Al–CO_2 batteries with Al foil anodes, ionic liquid electrolytes, and NPG@Pd cathodes. The total reaction of batteries obeyed the following reaction: $4Al + 9CO_2 \leftrightarrow 2Al_2(CO_3)_3 + 3C$. Low discharge–charge overpotential of 0.091 V was observed, and remarkable energy efficiencies reached 87.7%. However, the discharge terminal voltage dropped from 0.72 to 0.57 V after 10 h of cycling, thus resulting in undecomposed discharge products. Herein, additional investigations on the improvement of cathode catalysts and electrolytes should be conducted.[121]

3.4. Zn–CO_2 Batteries

Different from Li–CO_2 and Na–CO_2 batteries, Zn–CO_2 batteries are likely to generate abundant discharge products, such as CO or formic acid. This unique merit provides a practical approach to deal with the blockage problem of indissoluble discharge products and improve reversibility. Yang et al. designed a type of trifunctional Ni–N/P–O-codoped grapheme (NiPG) electrocatalyst and applied it on Zn–CO_2 batteries. The synergistic effect of P–O and Ni–N units efficiently suppressed HER during the CRR process. Furthermore, these units manifested significant stability over 12 h discharge–charges cycles. After discharge, one of the main products was CO, and its Faradaic efficiency reached 66% at 1.5 mA cm^{-2}.[122] Hou et al. first applied single-atom catalysts (SACs) on the improvement of Zn–CO_2 batteries
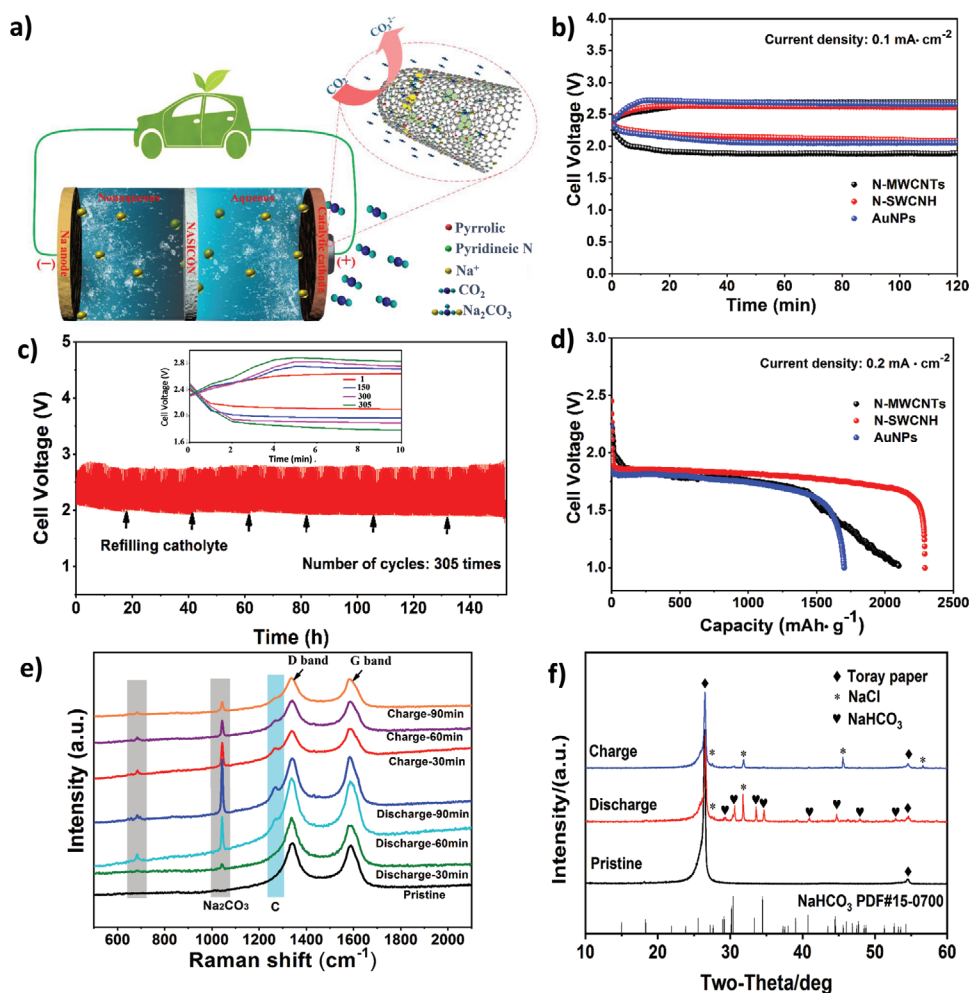
ADVANCED
SCIENCE NEWS
www.advancedsciencenews.com

NANO · MICRO
small
www.small-journal.com

Figure 12. a) Schematic of the proposed hybrid Na–CO$_2$ battery with N-SWCNH as a catalyst. b) Discharge–charge voltage curves with different catalysts at a current density of 0.1 mA cm^{-2}. c) The cycling performance of hybrid Na–CO$_2$ battery at a current density of 0.1 mA cm^{-2}. d) Discharge capacity curves at a current density of 0.2 mA cm^{-2}. e) In situ Raman characterization and f) ex situ XRD pattern of the hybrid Na-CO$_2$ battery during discharge and recharge. Reproduced with permission.[98] Copyright 2019, Elsevier.

by utilizing the gas diffusion strategy to locate Fe atoms on N-doped carbon (Fe$_1$NC/S$_1$-1000). This catalyst exhibited a high tendency to reduce CO$_2$ to CO and a remarkable TOF of 2225 h^{-1}, which exceeded most of the transition metal catalysts. Furthermore, compared with the previous research, Fe$_1$NC/S$_1$-1000 displayed high CO Faradaic efficiency of up to 96% with relatively low overpotential. The DFT results indicated that Fe-N$_3$ sites were the active sites of catalysts and possessed the capability to balance the energy barrier of each step during the CRR process. Therefore, the entire battery was endowed with a high power density of 526 mW cm^{-2} due to the aforementioned outstanding traits.[132] Xie et al. took 3D porous Pd containing interconnected nanosheet, enriched edge, and pore structure to form reversible aqueous Zn–CO$_2$ battery (**Figure 14**a). Formic acid was proven to be major discharge products with high Faradaic efficiency of over 90% at a current density of 15 mA cm^{-2} (Figure 14b). The reaction mechanism of formic acid was Zn + CO$_2$ + 2H$^+$ + 2OH$^-$ ↔ ZnO + HCOOH + H$_2$O. Herein, the repeating utilization capability of CO$_2$ was substantially

promoted. The discharge–charge overpotential maintained 0.54 V (Figure 14c) and the battery remained durable over 100 cycles after 10 h operation (Figure 14d).[23]

In addition to formic acid and CO, methane was recently reported as a high valued discharge product. Hu et al. designed the complete flow of a Zn–CO$_2$ battery device, which was different from traditional close battery systems. This battery comprised carbon hollow fiber (CHF) cathode, metallic Zn wire anode, and [EMIM][BF$_4$] electrolyte. Inflowing CO$_2$ was reduced to methane with remarkable Faradaic efficiency of 94%, and methane flowed out through CHF effectively. Oxidized Zn anode was further electroreduced by other types of renewable energy. The entire battery generated a high energy density of 288.3 Wh kg^{-1} and remained stably discharged for eight days. High selectivity and electrochemical performance attributed to the availability of protons are ensured by the water shuttle between anodes and [EMIM][BF$_4$]. Furthermore, [EMIM]$^+$ as an electrolyte played a crucial role in the adsorption of CO$_2$ to reduce kinetic barriers. The exquisite design

ADVANCED
SCIENCE NEWS
www.advancedsciencenews.com
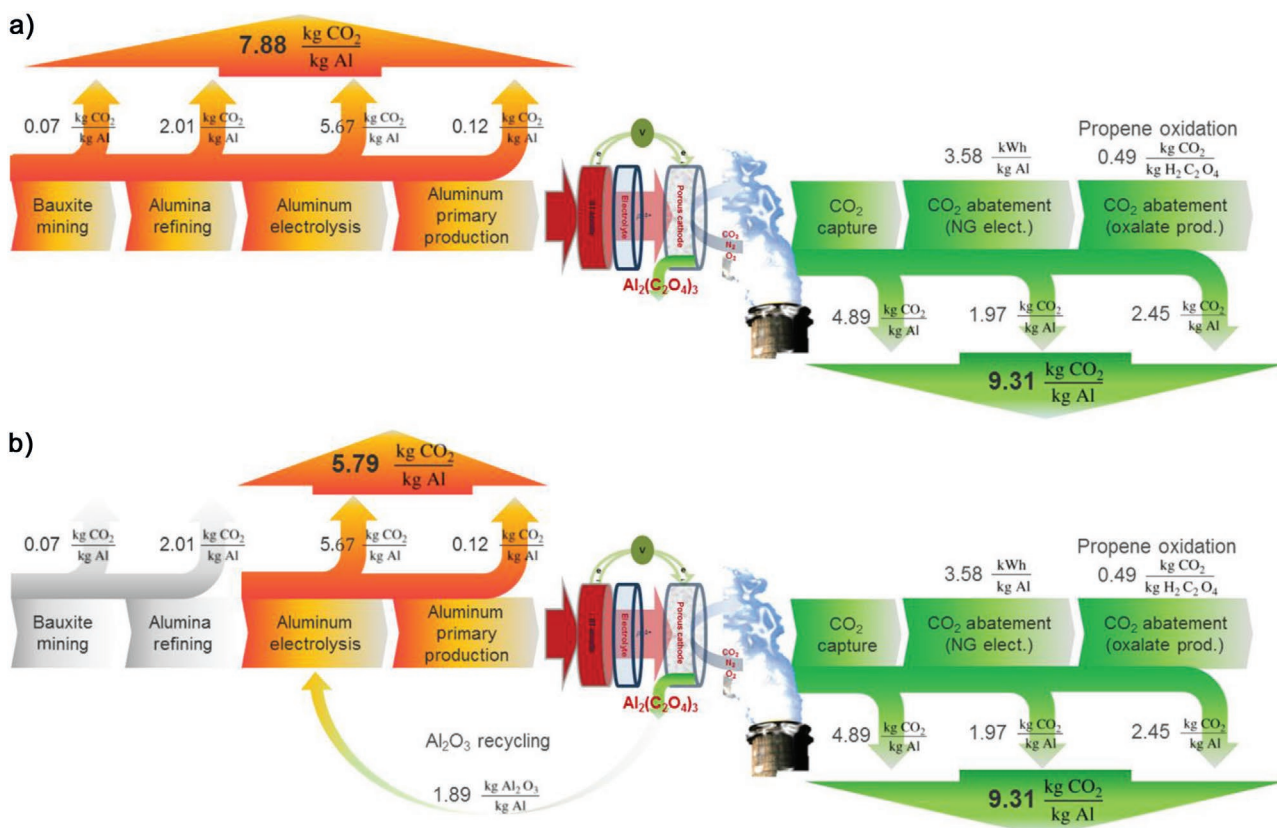
NANO · MICRO
small
www.small-journal.com

Figure 13. Preliminary system analysis. a) Overall balance of CO_2 emissions captured/abated by the primary Al/80% CO_2 electrochemical system contrasted with emissions of aluminum metal production. b) Overall balance of CO_2 emissions, allowing the recycling of Al_2O_3 for aluminum metal production. Reproduced with permission.[120] Copyright 2016, American Association for the Advancement of Science.

of the Zn–CO_2 battery implemented the effective conversion of CO_2 to flues and generated electric power simultaneously. Zn–CO_2 flow battery shouldered the responsibility of inhibiting green gas production with the continuous regeneration of the Zn anode.[123]

4. Electroreduction of CO_2 to Carbonaceous Fuels

Converting CO_2 into fuel is widely considered to be one of the practical and attractive means to deal with energy shortage and maintain carbon balance. Therefore, high energy density fuels, such as methane and ethanol, were manufactured by utilizing CO_2 as raw material.[133] However, the selectivity of products is the major problem for CRR improvement.[134] Electrocatalyst design is crucial in the reaction and selectivity rates of products during the CO_2 electroreduction process. Different from metal-CO_2 batteries, the entire reaction occurs in electrolytic cells. Many issues should be considered to obtain ideal products: the bond strength with adsorbed elements, the competitiveness of HER, and the energy barrier of electron transformation. Furthermore, some intermediates, such as $CO_2{}^{·-}$, *COOH, CHO, and COH, have different absorption energies with the catalyst surface, which determines product formation pathways and affects final products. The electroreduction process can be detected through state-of-the-art techniques,

such as DFT and in situ analysis. This process is critical in the tuning of active sites and the design of effective electrocatalysts. The catalytic performance and selectivity of various catalysts are comprehensively summarized in **Figure 15**.

4.1. Production of CO

In most CO formation processes, CO_2 should be initially reduced to $CO_2{}^{·-}$ radical and adsorbed on the catalyst surface.[135] The adsorbed $CO_2{}^{·-}$ radical is then converted into *COOH intermediate in aqueous solutions. Finally, *COOH is reduced to the final product of CO. Catalysts should generate stable bonds with $CO_2{}^{·-}$ to obtain satisfactory catalytic efficiency. Simultaneously, these catalysts should quickly desorb CO to prevent further reduction and catalyst poisoning.[136]

Au and Ag are considered to be the preferred catalysts to convert CO_2 into CO due to the weak CO bond.[137] However, their catalytic capabilities are limited by the low local concentration of CO_2 because adsorbed CO_2 is incapable of forming non-covalent interactions with noble metal surfaces. Shi et al. developed an Au/C three-phase contact system and reformed it via wettability-control to solve the aforementioned issue. This system displayed a high CO_2 mass-transfer coefficient of 0.27 cm s^{-1}, and its CO current density reached 99.9 mA cm^{-2} at –0.48 V versus RHE.[138] Bimetallic catalyst, especially Cu–Sn bimetallic catalyst, is also
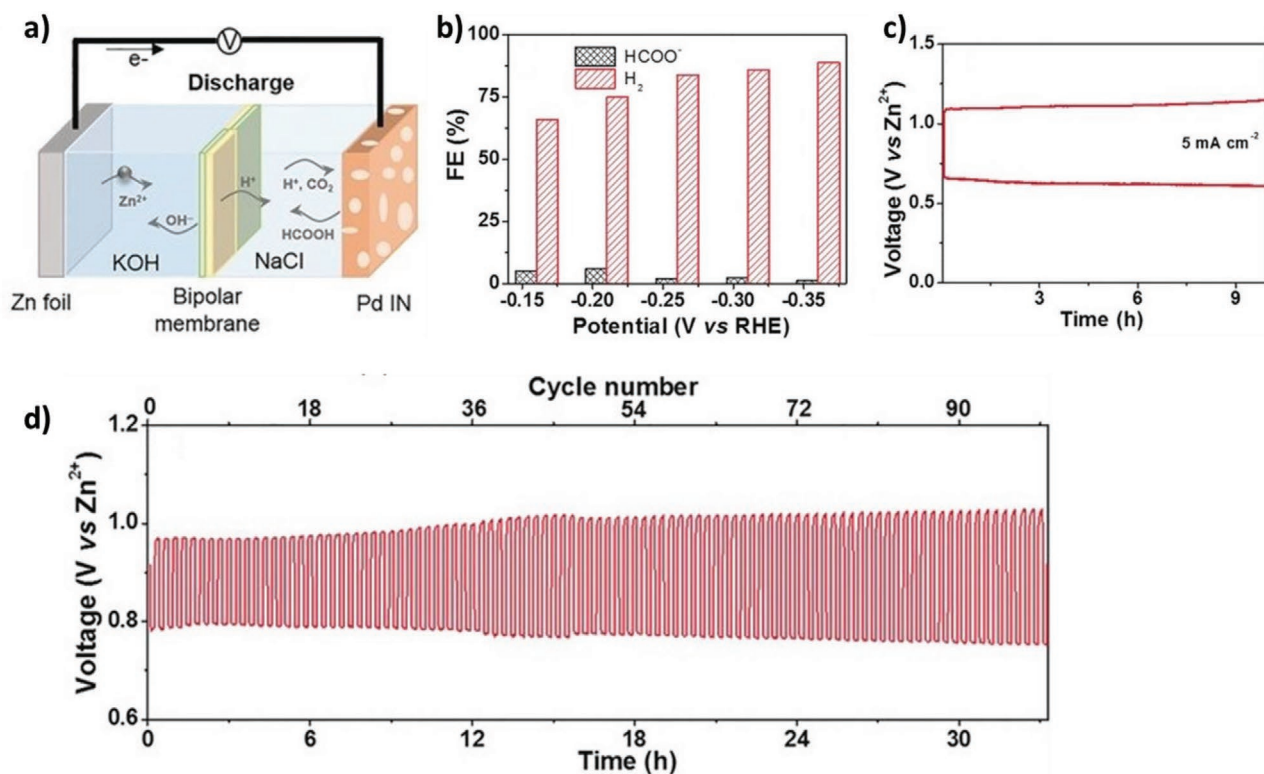
ADVANCED
SCIENCE NEWS
www.advancedsciencenews.com

NANO · MICRO
small
www.small-journal.com

Figure 14. a) Schematic representation of the reversible aqueous Zn–CO_2 battery. b) Faradaic efficiency of CO_2-to-HCOOH conversion and competitive HER. c) Prolonged galvanostatic discharge curve at 5 mA cm−2. d) Galvanostatic discharge–charge cycling curves at 0.56 mA cm−2. Reproduced with permission.[23] Copyright 2018, Wiley-VCH.
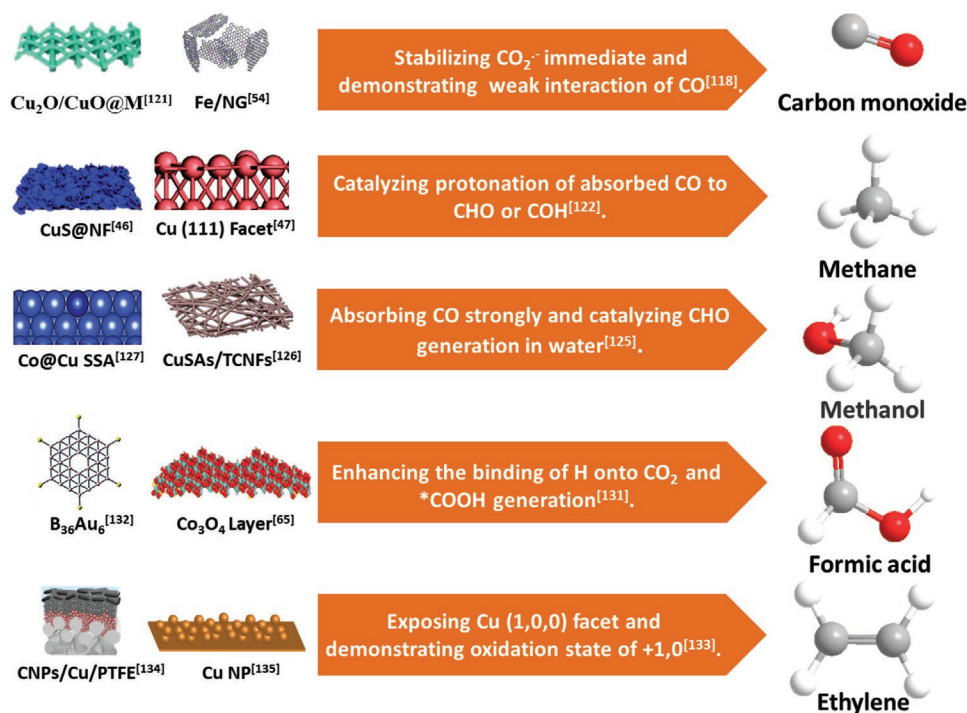

Figure 15. Catalysts with different traits catalyze the transformation of CO_2 to certain products.

ADVANCED
SCIENCE NEWS
www.advancedsciencenews.com

NANO · MICRO
small
www.small-journal.com

widely used as effective electrocatalysts. The Faradaic efficiency of CO is larger than 90% with low overpotential because the unique structure of the bimetallic catalyst assists the catalyst surface in inhibiting the adsorption of *H and bond *COOH intermediate effectively.[139] In addition, metal oxides exhibit outstanding performance. Yang et al. reported that $Cu_2O/CuO@$ Ni nanowires strengthened the adsorption of *COOH and had high selectivity to CO (95%) due to the synergistic effect between Cu_2O/CuO nanowires and Ni nanoparticles.[140]

4.2. Production of Methane

Only a small amount of catalysts, which can maintain high and stable methane selectivity, is currently available. Among them, transition metals, especially Cu, exhibit the most excellent catalytic performance on the selectivity of methane. The protonation of adsorbed CO is the most decisive step considering overpotential. Thus, strong bonding with CHO or COH intermediate is critical for the catalyst surface to increase the potential of the protonate CO. Furthermore, the competition of HER is a tricky problem due to the similarity of standard potential.[141] Five strategies are utilized to improve the catalytic capability of protonation: 1) alloying with metals processing high oxygen affinity, 2) electrophilic ligand stabilization, 3) tethering of ligands, 4) addition of promoters, and 5) hydrogen bond stabilization/solvent effects.[142] According to the volcano plot, Cu shows less protonation overpotential compared with other metals. Qiu et al. fabricated the Cu electrode via pulse electrodeposition. The transfer of electrons to CO_2 was strengthened due to the presence of a stepped surface, which reduced the energy barrier of CRR and exhibited high methane Faradaic efficiency of up to 85% at −2.8 V.[58]

4.3. Production of Methanol

CO_2 is reduced to CO and is adsorbed on the catalyst surface during the entire process of CO_2 electroreduction to methanol.[143] Adsorbed CO is then reduced to CHO*, CH_2O*, and CH_3O*. Products are eventually desorbed from the surface to fabricate methanol.[144]

Using first-principles calculations, researchers predicated that Cu-based single-atom alloy is an ideal electrocatalyst for methanol production. Moreover, narrowed Co d-band bonded with COH* stably after the addition of Co atoms into the catalyst, which is beneficial to further reduction reaction.[145] Yang et al. employed Cu SAC on CRR by decorating Cu atoms on through-hole carbon nanofiber (CuSAs/TCNF), which revealed the Faradaic efficiency of CH_3OH at 44% and remained stable after 50 h test.[143] In addition to Cu, Zhao et al. reported that FeS_2/NiS nanocomposite contained active sites between FeS_2 and NiS, which effectively suppressed HER and maintained high CH_3OH Faradaic efficiency of 64% after 4 h operation.[146]

4.4. Production of Formic Acid/Formate

In CRR history, formic acid/formate was reported by Royer to be the first final product of CRR in 1870.[147] From the viewpoint of DFT, the most crucial step of CO_2 reduction to formic acid/formate is to bond hydrogen onto CO_2 molecules to form HCOO* or OCHO* intermediates. The final product of formic acid/formate is generated by the reduction in HCOO* intermediate.[12b,148] *OCHO is a better electron-withdrawing group compared with *COOH. Hence, catalysts containing electron donors are likely to bond with *OCHO and perform further charge transfer. Moreover, the Gibbs free energy of *OCHO formation was 0.59 eV less than that of *COOH based on the DFT data.[149]

Due to favor adsorption of *OCHO over HCOO*, Sn- and Bi-based catalysts are considered as promising candidates to product formate.[150] Liu et al. recently synthesized Ga-Sn alloys, via a novel mean of solid–liquid phase transition from Sn–In alloys. The crystallization of Ga–Sn alloys exhibited great adsorption of *OCHO. Based on this attribute, formate Faradaic efficiency of Ga–Sn alloys reached 95%, which was nearly threefold than original Sn–In alloys.[151] Fan et al. reported the morphology of Bi nanomaterial, especially curvature, had large impact on the selectivity of formate. Bi nanotube exhibited larger formate Faradaic efficiency of 97% than that of Bi nanosheet (95%), owing to high energy barrier of HER on Bi nanotube surface.[152]

4.5. Production of Ethylene

Similar to methane, Cu-based catalysts exhibit the highest efficiency of CO_2 reduction to ethylene. The dimerization of carbon atoms during the entire reaction process is the rate-determining step of the C_2 compound formation, which almost occurs on the Cu(100) facet.[153] Moreover, Cu^0 and Cu^+ enhance the adsorption and stabilization of intermediates and further improve the product selectivity.[154]

The addition of iodine atoms employs halides and cationic Cu species, collaborating with rough surface morphology, form defects, and low-coordinated sites to promote C–C coupling. Herein, the iodine-modified catalyst displays the highest ethylene Faradaic efficiency of 80%.[155] Moreover, hydrophilic ionomer loaded on polycrystalline Cu surfaces establishes pathways to increase CO_2 diffusion substantially and optimize reaction kinetics. Compared with bare Cu catalysts, the CRR current density increases from 50 to 510 mA cm^{-2} due to the synergetic effect of Cu nanoparticles and ionomer, and ethylene Faradaic efficiency is still larger than 40% after 60 h test.[156]

4.6. Production of Methylglyoxal

To date, 1-propanol, acetone, and methylglyoxal are reported to be common C_3 products of CRR. However, most C_3 synthesis is plagued by problems of low Faradaic efficiency, most of which are less than 10%, and unclear reaction mechanism.[157] Notably, detailed process steps of CO_2 electroreduction to methylglyoxal was discovered by Dismukes et al. Adsorbed CO_2 was transformed to *HCOO− during the reaction and then protonated to generate H_2CO* immediate. Afterward, two steps of self-condensation reactions occurred and converted H_2CO* into
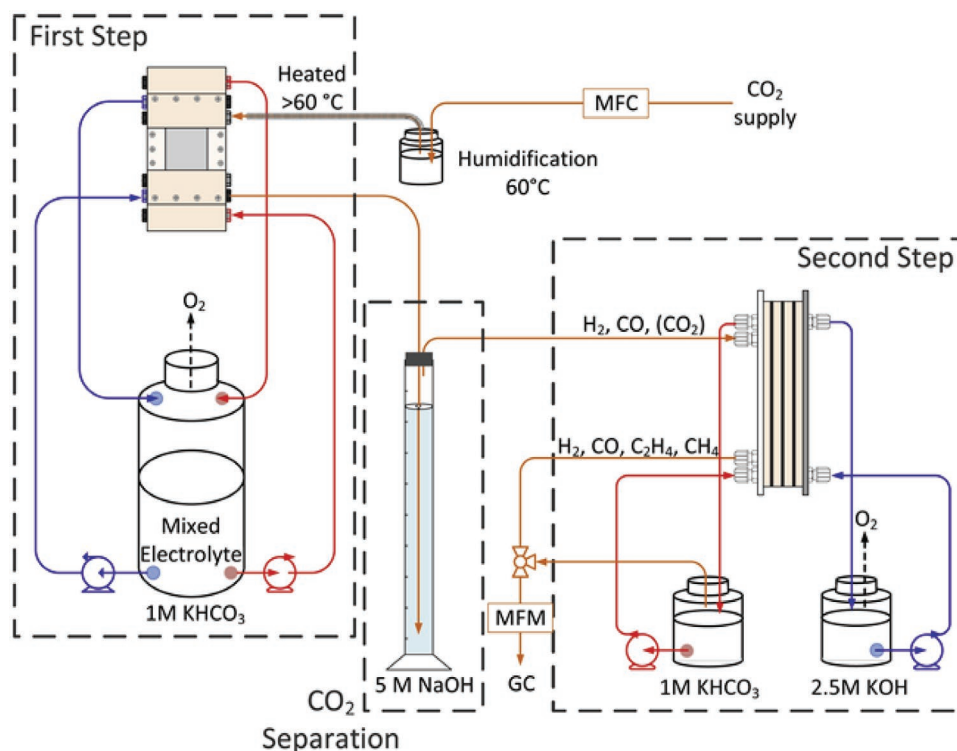
Figure 16. Schematic of the two-step CRR method. Reproduced with permission.[165] Copyright 2020, Elsevier.

glyceraldehyde. Eventually, glyceraldehyde reacted with H_2O molecules in electrolytes and generated the final methylglyoxal product.

Moreover, researchers obtained a maximum methylglyoxal Faradaic efficiency of 84% when Ni_2P was applied to the methylglyoxal formation at a relative positive potential of −0.1 V versus RHE. The remarkable methylglyoxal Faradaic efficiency rendered promising means to manufacture C_3 products.[158]

5. Practical Application of CO_2 Electroreduction

From theoretical viewpoint, practical CRR application exhibits excellent economic benefits. For instance, by using industrial electricity the cost of electroreducing CO_2 to ethanol is about \$0.32 L^{-1}, which is less than 2020 average fuel ethanol price of \$0.38 L^{-1}.[159] Moreover, governments provide substantial financial support to promote CRR industrial application, such as "Rheticus project" of Germany, "CO_2perate" of Belgium, and "Recode" of Italy.[160]

Regrettably, totally industrial CRR technology still does not exist, but some technologies have entered the pilot stage.[160] Among them, converting CO_2 into CO is the most mature technology.[161] Haldor Topsøe developed high-temperature CO_2 electroreduction system, which successfully produced 96 Nm^3 h^{-1} and synthesized CO with purity of 99.95%.[162] Different from high-temperature system, Schmid et al. introduced a type of low-temperature electrolyzers. During the process, humid CO_2 was injected into cathode and then syngas, mixing above 30% CO with H_2, was finally produced, which kept stable after 650 h test.[163]

Compared with CO generation, electroreduction of CO_2 to formic acid and C_2 products is further away from commercialization, due to the limitation of catalyst stability and complicated reaction mechanism.[164] Herein, two-step method is introduced as a promising mean to achieve industrial C_2 production. During the process, CO_2 is electroreduced to CO to form CO/CO_2 syngas in the first step, and CO is further transferred to hydrocarbons in the second step (**Figure 16**).[165] Schmid et al, innovated this system to enhance energy efficiency and environmental friendliness. In this system, solar cell was used as power source and biological fermentation was used to convert syngas. Multiple alcohols, including ethanol, butanol, and hexanol, were synthesized successfully, with nearly 100% desired alcohols Faradaic efficiency. Furthermore, the new system was able to work continuously at 300 mA cm^{-2} for 200 h.[166]

Compared with relatively mature CRR electrolyzers, metal-CO_2 batteries are still in its infancy. Whereas, with the progress of catalysts, electrolyte, and electrode material, metal-CO_2 batteries possess potential application value in the future. As mentioned in Section 4, Li/Na–CO_2 and Zn/Al–CO_2 systems have different electrochemical properties, with respective application directions. Due to brilliant energy density and capacity, Li/Na–CO_2 system is hopefully used as vehicle batteries, especially Mars exploration whose 95% atmosphere is CO_2.[167] On the other hand, with low price of anode and high valued discharge products, Zn/Al–CO_2 system can be taken as primary batteries on industry exhaust treatment and realize carbonaceous compound production with negative energy.

6. Conclusion and Outlook

Aiming to identify a promising and practical pathway for energy conversion, this review concluded two major applications of CRR: energy generation by metal–CO_2 batteries and electroreduction of CO_2 to carbonaceous fuel. Among all influence factors, electrocatalysts play a decisive role in the activity and selectivity of the two applications. The recent development of electrocatalysts employed in the two applications is reviewed. Moreover, this review provides a clear cognition of the selection of suitable CRR catalysts in the future by comparing their catalytic capabilities.

However, numerous challenges must be overcome to accomplish the industrial application of CRR. Several future directions from the aspects of two applications are comprehensively presented in the following paragraph.

1) Employing single-atom catalysts (SACs)

The SACs have attracted considerable attention. Ordinarily, the formation of SAC aims to combine substrate and single-atom sites via confinement effect.[168] The coordinated effects of substrate adjust single-atom sites considering shape, composition, structure, and catalytic performance.[169] Moreover, single-atom sites of SACs endow catalysts with some traits of homogeneous catalysts, such as remarkable TOF numbers.[170] The size of single atoms means that SACs take advantage of providing a large amount of contact surface with CO_2 molecule. SACs exhibit different traits from conventional catalysts by doping atoms belonging to metal atoms. For instance, theoretical calculation results reveal that the synergistic effect of the p-orbital of graphene and d-orbital of metal atoms strengthens specific intermediate bonds, such as *CHO, and then CRR selectivity was enhanced to a large extent.[31] Therefore, compared with nanoparticles containing different shapes, sizes, and configurations, single-atom sites significantly enhanced the selectivity of catalysts.[171] Moreover, the discovery of effective substrates instead of carbon-based supports is important. Sun et al. loaded Pt atoms on octahedral Pd crystals to form alloys and then deposited them on CNTs via atomic layer deposition. This method prevented the effective oxidation of Pt atoms, which introduced a new direction of a novel type of SACs.[172]

2) Application of operando techniques on deep analysis

Most of the existing measurements may introduce erroneous data because many reactions should be performed under certain conditions. Furthermore, these testing methods help researchers identify reaction roadmaps and intermediates. Although calculations of quantum chemistry can analyze the transformation of adsorbed reactants, handling relatively new and complicated systems is difficult.[173] The operando techniques can analyze the activity and selectivity of catalysts synchronously, while reaction conditions are close to real working environments.[174] This study presents a clear and innovative insight into the reaction mechanism and formation of different intermediates by operando techniques.[175] For instance, Pd lattice was inserted by hydrogen and transformed to PdH during the CRR through the operando XAS spectra.[176] In situ infrared spectroscopy (SEIRAS) was recently applied to the testing of local pH near electrode surfaces. Concentration gradients between electrodes and electrolytes are reported to have large impacts on reaction selectivity and activity, which offers inspiration for cell design in the future.[177]

3) Catalytic performance enhancement via plasma

Plasma, which is an ionized gas comprising electrons, ions, and neutral species, is an effective way used for material synthesis and modification. Nonthermal plasma is a nonequilibrium state at the temperature of 300–1000 K.[178] From the viewpoints of promoting reaction, plasma plays an important auxiliary role in the following two aspects: synergistic catalytic and catalyst surface modification. Synergistic catalytic means that plasma participates in the reaction process and affects reaction pathways. Plasma protects catalysts from being poisoned during the entire reaction by modifying product desorption and increasing the rate of product formation.[179] In addition, catalyst surface modification is a vital use of plasma considering material modification. Strong effects of etching, sputtering, charging, and heating may occur during plasma interaction with catalyst surfaces. Herein, morphology and oxidation state on surfaces may substantially change and generate large active surface areas.[178] Therefore, catalyst surface modification by plasma improves the activity and selectivity of catalysts on the CRR catalytic process.[180] For example, plasma peroxide Ag surface exhibits a strong bonding of reaction intermediate and has superior selectivity to CO.[181]

4) Theoretical research via machine learning

The recent application of machine learning on DFT calculation, organic synthesis, and catalyst design is appealing.[182] Considering catalyst design, machine learning plays the main role in predicting catalysts with high selectivity based on massive data in the silico database.[183] A surrogate model is established during the process of machine learning to select suitable data, and the data are taken into the original database to loop multiple times. Finally, the model will become increasingly ideal. Furthermore, genetic algorithms, which exhibit strong information selection capability and evolution participation of catalysts, are utilized in the model by mimicking biology.[184] The combination of machine learning with other calculation methods increases calculation efficiency to a large extent. Machine learning collaborates with surrogate-based optimization through the DFT database to analyze metals comprehensively, which has near-optimal bond energy with adsorbates, such as CO. The time consumption of theoretical calculation and experiment is reduced in the present study to a large extent.[185]

5) Improvement of metal–CO_2 batteries

As the emerging fields of energy storage devices, many aspects of metal–CO_2 batteries must still be improved: high overpotential, unstable ion transport, and low safety. First, many discharge products of metal–CO_2 batteries are carbonates, which are not decomposed easily and has poor electronic conduction.[186] Herein, alternating carbonates with other carbonaceous products may be a future trend. The first attempt was

ADVANCED
SCIENCE NEWS
www.advancedsciencenews.com

NANO · MICRO
small
www.small-journal.com

performed on primary Zn–CO$_2$ batteries, which reduced CO$_2$ to CO with a low discharge–charge overpotential of 0.2 V.[23] However, other metal-CO$_2$ batteries that exhibit the same properties currently remain unreported, thus deserving additional attention.[110b] Furthermore, many metal–CO$_2$ batteries face the common problem of irregular ion transport and dendritic deposition due to the unstable hydrodynamics of liquid electrolytes.[187] Different from liquid electrolytes, solid electrolytes provide ions with stable transmission channels based on tuning structure and composition of crystals.[188] Therefore, quasi-solid batteries will become appealing and promising candidates for next-generation batteries after overcoming problems of interfacial kinetics and mechanical property.[189] Finally, another key issue inhibiting the development of metal–CO$_2$ batteries is the high instability of active metal anodes, such as Na and Li, which may introduce considerable security risks. The application of liquid anodes is considered to be one of the practical solutions, which usually is formed by dissolving metals into organic solvents, such as biphenyl and ethers.[190] Some works have been implemented on Na–air batteries, thus demonstrating its remarkable potential in the field of metal–CO$_2$ batteries.[191]

6) Novel design of CRR electrolyzer

Utilizing CRR on the mass production of carbonaceous fuels is one of the vital goals of new energy exploration. However, compared with laboratory experiments, industrial applications may face complex conditions, which may weaken the stability and activity of reactors. Traditional H-type electrolyzers can only work for tens of hours and exhibit a limited current density of 100 mA cm^{-2}, which does not meet the industrial production requirement.[192] Thus, the membrane electrode assembly cell (MEA), which comprises the gas diffusion electrode (GDE) and ion-exchange membrane, is introduced to solve these problems. GDE plays a key role in improving the kinetics condition of cathode due to its macroscale pores by maintaining stable gas diffusion and remarkable electron conductivity.[193] Additional contributions of GDE include flexible configuration of various membranes, which enhance specific ion movement and impurity of products.[194] Xia et al. used MEA cells to convert CO$_2$ into formic acid, with high Faradaic efficiency exceeding 90%. The reactor was reported to generate 12 M formic acid solution and produce 0.1 M formic acid stably for 100 h.[195]

Overall, in the future, CRR application shows potential in the fields of environment protection, energy conversion, and space exploration.

Acknowledgements

Conflict of Interest

The authors declare no conflict of interest.

[1] L. Zhang, Z. J. Zhao, J. Gong, *Angew. Chem., Int. Ed. Engl.* **2017**, *56*, 11326.

[2] a) M. Halmann, *Nature* **1978**, *275*, 115; b) X. C. Duan, J. T. Xu, Z. X. Wei, J. M. Ma, S. J. Guo, S. Y. Wang, H. K. Liu, S. X. Dou, *Adv. Mater.* **2017**, *29*, 1701784.

[3] A. Houmam, *Chem. Rev.* **2008**, *108*, 2180.

[4] a) M. Ma, B. J. Trzesniewski, J. Xie, W. A. Smith, *Angew. Chem., Int. Ed.* **2016**, *55*, 9748; b) R. Francke, B. Schille, M. Roemelt, *Chem. Rev.* **2018**, *118*, 4631.

[5] a) M. Bourrez, F. Molton, S. Chardon-Noblat, A. Deronzier, *Angew. Chem., Int. Ed. Engl.* **2011**, *50*, 9903; b) S. Zhang, Q. Fan, R. Xia, T. J. Meyer, *Acc. Chem. Res.* **2020**, *53*, 255.

[6] R. Francke, R. D. Little, *Chem. Soc. Rev.* **2014**, *43*, 2492.

[7] a) Z.-Y. Zhou, S.-G. Sun, *Natl. Sci. Rev.* **2016**, *4*, 155; b) S. Back, H. Kim, Y. Jung, *ACS Catal.* **2015**, *5*, 965.

[8] H. Jiang, Y. M. Zhao, L. Z. Wang, Y. Kong, F. Li, P. Li, *J. CO2 Util.* **2018**, *26*, 408.

[9] M. Gattrell, N. Gupta, A. Co, *J. Electroanal. Chem.* **2006**, *594*, 1.

[10] J. H. Wu, Y. Huang, W. Ye, Y. G. Li, *Adv. Sci.* **2017**, *4*, 1700194.

[11] a) R. L. Cook, R. C. Macduff, A. F. Sammells, *J. Electrochem. Soc.* **1990**, *137*, 607; b) Y. Nishimura, D. Yoshida, M. Mizuhata, K. Asaka, K. Oguro, H. Takenaka, *Energy Convers. Manage.* **1995**, *36*, 629; c) R. L. Cook, *J. Electrochem. Soc.* **1990**, *137*, 607.

[12] a) N. S. Spinner, J. A. Vega, W. E. Mustain, *Catal. Sci. Technol.* **2012**, *2*, 19; b) W. Zhang, Y. Hu, L. Ma, G. Zhu, Y. Wang, X. Xue, R. Chen, S. Yang, Z. Jin, *Adv. Sci.* **2018**, *5*, 1700275.

[13] X. F. Hu, Z. F. Li, Y. R. Zhao, J. C. Sun, Q. Zhao, J. B. Wang, Z. L. Tao, J. Chen, *Sci. Adv.* **2017**, *3*, e1602396.

[14] a) N. Mohd Adli, W. Shan, S. Hwang, W. Samarakoon, S. Karakalos, Y. Li, D. A. Cullen, D. Su, Z. Feng, G. Wang, G. Wu, *Angew. Chem., Int. Ed.* **2021**, *60*, 1022; b) L. Fan, C. Xia, F. Yang, J. Wang, H. Wang, Y. Lu, *Sci. Adv.* **2020**, *6*, eaay3111; c) S. Popović, M. Smiljanić, P. Jovanovič, J. Vavra, R. Buonsanti, N. Hodnik, *Angew. Chem.* **2020**, *132*, 14844; d) D. Yang, B. Ni, X. Wang, *Adv. Energy Mater.* **2020**, *10*, 2001142; e) H. Zhang, W. Cheng, D. Luan, X. W. Lou, *Angew. Chem., Int. Ed.* **2021**, *60*, 2; f) Y. Wang, Y. Liu, W. Liu, J. Wu, Q. Li, Q. Feng, Z. Chen, X. Xiong, D. Wang, Y. Lei, *Energy Environ. Sci.* **2020**, *13*, 4609.

[15] a) X. Mu, X. Pan, P. He, H. Zhou, *Adv. Mater.* **2020**, *32*, 1903790; b) Z. Zhang, W.-L. Bai, K.-X. Wang, J.-S. Chen, *Energy Environ. Sci.* **2020**, *13*, 4717; c) B. Liu, Y. Sun, L. Liu, J. Chen, B. Yang, S. Xu, X. Yan, *Energy Environ. Sci.* **2019**, *12*, 887; d) Z. Xie, X. Zhang, Z. Zhang, Z. Zhou, *Adv. Mater.* **2017**, *29*, 1605891.

[16] a) D.-H. Nam, P. De Luna, A. Rosas-Hernández, A. Thevenon, F. Li, T. Agapie, J. C. Peters, O. Shekhah, M. Eddaoudi, E. H. Sargent, *Nat. Mater.* **2020**, *19*, 266; b) A. Wagner, C. D. Sahm, E. Reisner, *Nat. Catal.* **2020**, *3*, 775; c) Y. Y. Birdja, E. Pérez-Gallent, M. C. Figueiredo, A. J. Göttle, F. Calle-Vallejo, M. T. M. Koper, *Nat. Energy* **2019**, *4*, 732.

[17] E. E. Benson, C. P. Kubiak, A. J. Sathrum, J. M. Smieja, *Chem. Soc. Rev.* **2009**, *38*, 89.

[18] D. R. Kauffman, D. Alfonso, C. Matranga, H. Qian, R. Jin, *J. Am. Chem. Soc.* **2012**, *134*, 10237.

[19] S. Back, M. S. Yeom, Y. Jung, *J. Phys. Chem. C* **2018**, *122*, 4274.

[20] G. Hyun, J. T. Song, C. Ahn, Y. Ham, D. Cho, J. Oh, S. Jeon, *Proc. Natl. Acad. Sci. USA* **2020**, *117*, 5680.

[21] J. Rosen, G. S. Hutchings, Q. Lu, S. Rivera, Y. Zhou, D. G. Vlachos, F. Jiao, *ACS Catal.* **2015**, *5*, 4293.

[22] S.-Q. Liu, S.-W. Wu, M.-R. Gao, M.-S. Li, X.-Z. Fu, J.-L. Luo, *ACS Sustainable Chem. Eng.* **2019**, *7*, 14443.

[23] J. Xie, X. Wang, J. Lv, Y. Huang, M. Wu, Y. Wang, J. Yao, *Angew. Chem., Int. Ed. Engl.* **2018**, *57*, 16996.

[24] D. Kim, J. Resasco, Y. Yu, A. M. Asiri, P. Yang, *Nat. Commun.* **2014**, *5*, 4948.

[25] K. Liu, M. Ma, L. Wu, M. Valenti, D. Cardenas-Morcoso, J. P. Hofmann, J. Bisquert, S. Gimenez, W. A. Smith, *ACS Appl. Mater. Interfaces* **2019**, *11*, 16546.

[26] L. Lu, X. Sun, J. Ma, D. Yang, H. Wu, B. Zhang, J. Zhang, B. Han, *Angew. Chem., Int. Ed. Engl.* **2018**, *57*, 14149.

[27] D. Chen, Q. Yao, P. Cui, H. Liu, J. Xie, J. Yang, *ACS Appl. Energy Mater.* **2018**, *1*, 883.

[28] W. Zhu, R. Michalsky, O. Metin, H. Lv, S. Guo, C. J. Wright, X. Sun, A. A. Peterson, S. Sun, *J. American Chemical Society* **2013**, *30*, 1910534.

[29] Y. Zhu, J. Sokolowski, X. Song, Y. He, Y. Mei, G. Wu, *Adv. Energy Mater.* **2020**, *10*, 1902844.

[30] S. Back, M. S. Yeom, Y. Jung, *ACS Catal.* **2015**, *5*, 5089.

[31] S. Back, J. Lim, N. Y. Kim, Y. H. Kim, Y. Jung, *Chem. Sci.* **2017**, *8*, 1090.

[32] a) J. C. Calabrese, T. Herskovitz, J. B. Kinney, *J. Am. Chem. Soc.* **1983**, *105*, 5914; b) M. Aresta, C. F. Nobile, V. G. Albano, E. Forni, M. Manassero, *Chem. Informationsdienst* **1975**, *6*, 636; c) I. Castro-Rodriguez, H. Nakai, L. N. Zakharov, A. L. Rheingold, K. Meyer, *Science* **2004**, *305*, 1757.

[33] C. Kim, T. Eom, M. S. Jee, H. Jung, H. Kim, B. K. Min, Y. J. Hwang, *ACS Catal.* **2017**, *7*, 779.

[34] N. Austin, S. Zhao, J. R. McKone, R. C. Jin, G. Mpourmpakis, *Catal. Sci. Technol.* **2018**, *8*, 3795.

[35] H. Hadadzadeh, H. Farrokhpour, J. Simpson, J. Shakeri, M. Daryanavard, M. Shokrollahi, *New J. Chem.* **2016**, *40*, 6347.

[36] R. J. Lim, M. S. Xie, M. A. Sk, J. M. Lee, A. Fisher, X. Wang, K. H. Lim, *Catal. Today* **2014**, *233*, 169.

[37] J. F. Brennecke, B. E. Gurkan, *J. Phys. Chem. Lett.* **2010**, *1*, 3459.

[38] K. G. Schmitt, A. A. Gewirth, *J. Physical Chemistry C* **2014**, *118*, 17567.

[39] B. A. Johnson, S. Maji, H. Agarwala, T. A. White, E. Mijangos, S. Ott, *Angew. Chem., Int. Ed. Engl.* **2016**, *55*, 1825.

[40] K. Szkaradek, K. Buzar, E. A. Pidko, B. M. Szyja, *ChemCatChem* **2018**, *10*, 1814.

[41] a) B. Hammer, J. K. Norskov, *Nature* **1995**, *376*, 238; b) J. Hao, W. Shi, *Chin. J. Catal.* **2018**, *39*, 1157.

[42] H. Fei, J. Dong, Y. Feng, C. S. Allen, C. Wan, B. Volosskiy, M. Li, Z. Zhao, Y. Wang, H. Sun, P. An, W. Chen, Z. Guo, C. Lee, D. Chen, I. Shakir, M. Liu, T. Hu, Y. Li, A. I. Kirkland, X. Duan, Y. Huang, *Nat. Catal.* **2018**, *1*, 63.

[43] a) W. Ju, A. Bagger, G. P. Hao, A. S. Varela, I. Sinev, V. Bon, B. Roldan Cuenya, S. Kaskel, J. Rossmeisl, P. Strasser, *Nat. Commun.* **2017**, *8*, 944;. b) T. Möller, W. Ju, A. Bagger, X. Wang, F. Luo, T. Ngo Thanh, A. S. Varela, J. Rossmeisl, P. Strasser, *Energy Environ. Sci.* **2019**, *12*, 640; c) Z. Shi, W. Yang, Y. Gu, T. Liao, Z. Sun, *Adv. Sci.* **2020**, *7*, 2001069.

[44] T. N. Huan, N. Ranjbar, G. Rousse, M. Sougrati, A. Zitolo, V. Mougel, F. Jaouen, M. Fontecave, *ACS Catal.* **2017**, *7*, 1520.

[45] C. Zhang, S. Yang, J. Wu, M. Liu, S. Yazdi, M. Ren, J. Sha, J. Zhong, K. Nie, A. S. Jalilov, Z. Li, H. Li, B. I. Yakobson, Q. Wu, E. Ringe, H. Xu, P. M. Ajayan, J. M. Tour, *Adv. Energy Mater.* **2018**, *8*, 1703487.

[46] X. M. Hu, M. H. Ronne, S. U. Pedersen, T. Skrydstrup, K. Daasbjerg, *Angew. Chem., Int. Ed. Engl.* **2017**, *56*, 6468.

[47] G. Zhu, Y. Li, H. Zhu, H. Su, S. H. Chan, Q. Sun, *ACS Catal.* **2016**, *6*, 6294.

[48] P. Lu, Y. Yang, J. Yao, M. Wang, S. Dipazir, M. Yuan, J. Zhang, X. Wang, Z. Xie, G. Zhang, *Appl. Catal., B* **2019**, *241*, 113.

[49] M. Jia, C. Choi, T. S. Wu, C. Ma, P. Kang, H. Tao, Q. Fan, S. Hong, S. Liu, Y. L. Soo, Y. Jung, J. Qiu, Z. Sun, *Chem. Sci.* **2018**, *9*, 8775.

[50] I. Bhugun, D. Lexa, J.-M. Savéant, *J. Phys. Chem.* **1996**, *100*, 19981.

[51] a) D. Raciti, C. Wang, *ACS Energy Lett.* **2018**, *3*, 1545; b) N. J. Bernstein, S. A. Akhade, M. J. Janik, *Phys. Chem. Chem. Phys.* **2014**, *16*, 13708.

[52] A. Taheri, E. J. Thompson, J. C. Fettinger, L. A. Berben, *ACS Catal.* **2015**, *5*, 7140.

[53] A. N. Marianov, Y. Jiang, *Appl. Catal., B* **2019**, *244*, 881.

[54] A. N. Marianov, A. S. Kochubei, T. Roman, O. J. Conquest, C. Stampfl, Y. Jiang, *ACS Catal.* **2021**, *11*, 3715.

[55] Z. Zhao, Z. Chen, G. Lu, *J. Phys. Chem. C* **2017**, *121*, 20865.

[56] S. Nakagawa, A. Kudo, M. Azuma, T. Sakata, *J. Electroanal. Chem. Interfacial Electrochem.* **1991**, *308*, 339.

[57] Z. Zhao, X. Y. Peng, X. J. Liu, X. M. Sun, J. Shi, L. L. Han, G. L. Li, J. Luo, *J. Mater. Chem. A* **2017**, *5*, 20239.

[58] Y. L. Qiu, H. X. Zhong, T. T. Zhang, W. B. Xu, X. F. Li, H. M. Zhang, *ACS Catal.* **2017**, *7*, 6302.

[59] a) I. Takahashi, O. Koga, N. Hoshi, Y. Hori, *J. Electroanal. Chem.* **2002**, *533*, 135; b) Y. Hori, I. Takahashi, O. Koga, N. Hoshi, *J. Mol. Catal. A: Chem.* **2003**, *199*, 39.

[60] X. Zheng, Y. Ji, J. Tang, J. Wang, B. Liu, H.-G. Steinrück, K. Lim, Y. Li, M. F. Toney, K. Chan, Y. Cui, *Nat. Catal.* **2018**, *2*, 55.

[61] a) H. Yang, N. Han, J. Deng, J. Wu, Y. Wang, Y. Hu, P. Ding, Y. Li, Y. Li, J. Lu, *Adv. Energy Mater.* **2018**, *8*, 1801536; b) D. Yang, Q. Zhu, C. Chen, H. Liu, Z. Liu, Z. Zhao, X. Zhang, S. Liu, B. Han, *Nat. Commun.* **2019**, *10*, 677.

[62] K. Jiang, R. B. Sandberg, A. J. Akey, X. Liu, D. C. Bell, J. K. Nørskov, K. Chan, H. Wang, *Nat. Catal.* **2018**, *1*, 111.

[63] a) S. Nitopi, E. Bertheussen, S. B. Scott, X. Liu, A. K. Engstfeld, S. Horch, B. Seger, I. E. L. Stephens, K. Chan, C. Hahn, J. K. Nørskov, T. F. Jaramillo, I. Chorkendorff, *Chem. Rev.* **2019**, *119*, 7610; b) G. Henkelman, A. Arnaldsson, H. Jónsson, *Comput. Mater. Sci.* **2006**, *36*, 354.

[64] F. Li, A. Thevenon, A. Rosas-Hernandez, Z. Wang, Y. Li, C. M. Gabardo, A. Ozden, C. T. Dinh, J. Li, Y. Wang, J. P. Edwards, Y. Xu, C. McCallum, L. Tao, Z. Q. Liang, M. Luo, X. Wang, H. Li, C. P. O'Brien, C. S. Tan, D. H. Nam, R. Quintero-Bermudez, T. T. Zhuang, Y. C. Li, Z. Han, R. D. Britt, D. Sinton, T. Agapie, J. C. Peters, E. H. Sargent, *Nature* **2020**, *577*, 509.

[65] H. Wang, Y. K. Tzeng, Y. Ji, Y. Li, J. Li, X. Zheng, A. Yang, Y. Liu, Y. Gong, L. Cai, Y. Li, X. Zhang, W. Chen, B. Liu, H. Lu, N. A. Melosh, Z. X. Shen, K. Chan, T. Tan, S. Chu, Y. Cui, *Nat. Nanotechnol.* **2020**, *15*, 131.

[66] D. H. Nam, P. De Luna, A. Rosas-Hernandez, A. Thevenon, F. Li, T. Agapie, J. C. Peters, O. Shekhah, M. Eddaoudi, E. H. Sargent, *Nat. Mater.* **2020**, *19*, 266.

[67] a) C. W. Li, M. W. Kanan, *J. Am. Chem. Soc.* **2012**, *134*, 7231; b) C. W. Li, J. Ciston, M. W. Kanan, *Nature* **2014**, *508*, 504.

[68] Y. Lum, J. W. Ager, *Nat. Catal.* **2018**, *2*, 86.

[69] A. H. Shah, Y. Wang, S. Hussain, M. B. Akbar, A. R. Woldu, X. Zhang, T. He, *Phys. Chem. Chem. Phys.* **2020**, *22*, 2046.

[70] C. Peng, G. Luo, J. Zhang, M. Chen, Z. Wang, T.-K. Sham, L. Zhang, Y. Li, G. Zheng, *Nat. Commun.* **2021**, *12*, 1580.

[71] E. Tayyebi, J. Hussain, Y. Abghoui, E. Skúlason, *J. Phys. Chem. C* **2018**, *122*, 10078.

[72] H. Y. He, P. Zapol, L. A. Curtiss, *J. Phys. Chem. C* **2010**, *114*, 21474.

[73] S. Gao, X. Jiao, Z. Sun, W. Zhang, Y. Sun, C. Wang, Q. Hu, X. Zu, F. Yang, S. Yang, L. Liang, J. Wu, Y. Xie, *Angew. Chem., Int. Ed. Engl.* **2016**, *55*, 698.

[74] P. P. Yang, X. L. Zhang, F. Y. Gao, Y. R. Zheng, Z. Z. Niu, X. Yu, R. Liu, Z. Z. Wu, S. Qin, L. P. Chi, Y. Duan, T. Ma, X. S. Zheng, J. F. Zhu, H. J. Wang, M. R. Gao, S. H. Yu, *J. Am. Chem. Soc.* **2020**, *142*, 6400.

[75] D. D. Zhu, J. L. Liu, S. Z. Qiao, *Adv. Mater.* **2016**, *28*, 3423.

ADVANCED
SCIENCE NEWS

www.advancedsciencenews.com

NANO · MICRO
small
www.small-journal.com

[76] a) Z. Gu, N. Yang, P. Han, M. Kuang, B. Mei, Z. Jiang, J. Zhong, L. Li, G. Zheng, *Small Methods* **2018**, *3*, 1800449; b) H. Mistry, A. S. Varela, C. S. Bonifacio, I. Zegkinoglou, I. Sinev, Y.-W. Choi, K. Kisslinger, E. A. Stach, J. C. Yang, P. Strasser, B. R. Cuenya, *Nat. Commun.* **2016**, *7*, 12123.

[77] D. Ren, Y. Deng, A. D. Handoko, C. S. Chen, S. Malkhandi, B. S. Yeo, *ACS Catal.* **2015**, *5*, 2814.

[78] a) C. A. Trickett, A. Helal, B. A. Al-Maythalony, Z. H. Yamani, K. E. Cordova, O. M. Yaghi, *Nat. Rev. Mater.* **2017**, *2*, 17045; b) Q. Yang, Q. Xu, H.-L. Jiang, *Chem. Soc. Rev.* **2017**, *46*, 4774.

[79] a) R. Hinogami, S. Yotsuhashi, M. Deguchi, Y. Zenitani, H. Hashiba, Y. Yamada, *ECS Electrochem. Lett.* **2012**, *1*, H17; b) H. Zhang, J. Nai, L. Yu, X. W. Lou, *Joule* **2017**, *1*, 77.

[80] Y. L. Qiu, H. X. Zhong, T. T. Zhang, W. B. Xu, P. P. Su, X. F. Li, H. M. Zhang, *ACS Appl. Mater. Interfaces* **2018**, *10*, 2480.

[81] Y. R. Wang, Q. Huang, C. T. He, Y. Chen, J. Liu, F. C. Shen, Y. Q. Lan, *Nat. Commun.* **2018**, *9*, 4466.

[82] S. Dou, J. Song, S. Xi, Y. Du, J. Wang, Z. F. Huang, Z. J. Xu, X. Wang, *Angew. Chem.* **2019**, *58*, 4041.

[83] H. Liu, J. Chu, Z. Yin, X. Cai, L. Zhuang, H. Deng, *Chem* **2018**, *4*, 1696.

[84] S. Kandambeth, K. Dey, R. Banerjee, *J. Am. Chem. Soc.* **2019**, *141*, 1807.

[85] a) H. Furukawa, O. M. Yaghi, *J. Am. Chem. Soc.* **2009**, *131*, 8875; b) S.-Y. Ding, W. Wang, *Chem. Soc. Rev.* **2013**, *42*, 548.

[86] S. M. J. Rogge, A. Bavykina, J. Hajek, H. Garcia, A. I. Olivos-Suarez, A. Sepulveda-Escribano, A. Vimont, G. Clet, P. Bazin, F. Kapteijn, M. Daturi, E. V. Ramos-Fernandez, I. X. F. X. Llabres, V. Van Speybroeck, J. Gascon, *Chem. Soc. Rev.* **2017**, *46*, 3134.

[87] S. Lin, C. S. Diercks, Y.-B. Zhang, N. Kornienko, E. M. Nichols, Y. Zhao, A. R. Paris, D. Kim, P. Yang, O. M. Yaghi, C. J. Chang, *Science* **2015**, *349*, 1208.

[88] H. Jin, C. Guo, X. Liu, J. Liu, A. Vasileff, Y. Jiao, Y. Zheng, S. Z. Qiao, *Chem. Rev.* **2018**, *118*, 6337.

[89] Y. Liu, J. Zhao, Q. Cai, *Phys. Chem. Chem. Phys.* **2016**, *18*, 5491.

[90] S. Siahrostami, K. Jiang, M. Karamad, K. Chan, H. Wang, J. Nørskov, *ACS Sustainable Chem. Eng.* **2017**, *5*, 11080.

[91] P. Han, X. Yu, D. Yuan, M. Kuang, Y. Wang, A. M. Al-Enizi, G. Zheng, *J. Colloid Interface Sci.* **2019**, *534*, 332.

[92] P. P. Sharma, J. Wu, R. M. Yadav, M. Liu, C. J. Wright, C. S. Tiwary, B. I. Yakobson, J. Lou, P. M. Ajayan, X. D. Zhou, *Angew. Chem., Int. Ed. Engl.* **2015**, *127*, 13905.

[93] B. Kumar, M. Asadi, D. Pisasale, S. Sinha-Ray, B. A. Rosen, R. Haasch, J. Abiade, A. L. Yarin, A. Salehi-Khojin, *Nat. Commun.* **2013**, *4*, 2819.

[94] X. Zhang, Z. Wu, X. Zhang, L. Li, Y. Li, H. Xu, X. Li, X. Yu, Z. Zhang, Y. Liang, H. Wang, *Nat. Commun.* **2017**, *8*, 14675.

[95] Y. Guo, H. Yang, X. Zhou, K. Liu, C. Zhang, Z. Zhou, C. Wang, W. Lin, *J. Mater. Chem. A* **2017**, *5*, 24867.

[96] N. Karousis, I. Suarez-Martinez, C. P. Ewels, N. Tagmatarchis, *Chem. Rev.* **2016**, *116*, 4850.

[97] M. Melchionna, M. V. Bracamonte, A. Giuliani, L. Nasi, T. Montini, C. Tavagnacco, M. Bonchio, P. Fornasiero, M. Prato, *Energy Environ. Sci.* **2018**, *11*, 1571.

[98] C. Xu, K. Zhang, D. Zhang, S. Chang, F. Liang, P. Yan, Y. Yao, T. Qu, J. Zhan, W. Ma, B. Yang, Y. Dai, X. Sun, *Nano Energy* **2019**, *11*, 1571.

[99] C. Fang, J. Luo, C. Jin, H. Yuan, O. Sheng, H. Huang, Y. Gan, Y. Xia, C. Liang, J. Zhang, W. Zhang, X. Tao, *ACS Appl. Mater. Interfaces* **2018**, *10*, 17240.

[100] S. A. Goetz, D. T. Nguyen, A. P. Esser-Kahn, *Carbon* **2016**, *105*, 126.

[101] S. Xu, S. K. Das, L. A. Archer, *RSC Adv.* **2013**, *3*, 6656.

[102] Y. Liu, R. Wang, Y. Lyu, H. Li, L. Chen, *Energy Environ. Sci.* **2014**, *7*, 677.

[103] T. Liu, S. Ali, Z. Lian, C. Si, D. S. Su, B. Li, *J. Mater. Chem. A* **2018**, *6*, 19998.

[104] a) F. Pan, B. Li, W. Deng, Z. Du, Y. Gang, G. Wang, Y. Li, *Appl. Catal., B* **2019**, *252*, 240; b) H. P. Yang, Y. Wu, Q. Lin, L. D. Fan, X. Y. Chai, Q. L. Zhang, J. H. Liu, C. X. He, Z. Q. Lin, *Angew. Chem., Int. Edit.* **2018**, *57*, 15476.

[105] C. Chen, X. Sun, X. Yan, Y. Wu, H. Liu, Q. Zhu, B. B. A. Bediako, B. Han, *Angew. Chem., Int. Ed. Engl.* **2020**, *59*, 11123.

[106] a) X. Liu, L. Dai, *Nat. Rev. Mater.* **2016**, *1*, 16064; b) J. Masa, W. Xia, M. Muhler, W. Schuhmann, *Angew. Chem., Int. Ed.* **2015**, *54*, 10102; c) L. Wang, A. Ambrosi, M. Pumera, *Angew. Chem., Int. Ed.* **2013**, *52*, 13818.

[107] a) C. E. Banks, A. Crossley, C. Salter, S. J. Wilkins, R. G. Compton, *Angew. Chem., Int. Ed.* **2006**, *45*, 2533; b) A. Wuttig, Y. Surendranath, *ACS Catal.* **2015**, *5*, 4479.

[108] Y. Lum, Y. Kwon, P. Lobaccaro, L. Chen, E. L. Clark, A. T. Bell, J. W. Ager, *ACS Catal.* **2016**, *6*, 202.

[109] C. Kim, Y.-K. Choe, D. H. Won, U. Lee, H.-S. Oh, D. K. Lee, C. H. Choi, S. Yoon, W. Kim, Y. J. Hwang, B. K. Min, *ACS Energy Lett.* **2019**, *4*, 2343.

[110] a) K. Takechi, T. Shiga, T. Asaoka, *Chem. Commun.* **2011**, *47*, 3463; b) J. Xie, Y. Wang, *Acc. Chem. Res.* **2019**, *52*, 1721.

[111] J. Xie, Z. Zhou, Y. Wang, *Adv. Funct. Mater.* **2019**, *30*, 1908285.

[112] a) Y. Kang, F. M. Su, Q. K. Zhang, F. Liang, K. R. Adair, K. F. Chen, D. F. Xue, K. Hayashi, S. C. Cao, H. Yadegari, X. L. Sun, *ACS Appl. Mater. Interfaces* **2018**, *10*, 23748; b) F. Liang, X. C. Qiu, Q. K. Zhang, Y. Kang, A. Koo, K. Hayashi, K. F. Chen, D. F. Xue, K. N. Hui, H. Yadegari, X. L. Sun, *Nano Energy* **2018**, *49*, 574; c) F. Liang, T. Watanabe, K. Hayashi, Y. C. Yao, W. H. Ma, B. Yang, Y. N. Dai, *Mater. Lett.* **2017**, *187*, 32; d) W. Zhao, X. Li, R. Yin, L. Qian, X. Huang, H. Liu, J. Zhang, J. Wang, T. Ding, Z. Guo, *Nanoscale* **2019**, *11*, 50; e) J.-l. Ma, F.-l. Meng, Y. Yu, D.-p. Liu, J.-m. Yan, Y. Zhang, X.-b. Zhang, Q. Jiang, *Nat. Chem.* **2019**, *11*, 64.

[113] Y. Qiao, J. Yi, S. Wu, Y. Liu, S. Yang, P. He, H. Zhou, *Joule* **2017**, *1*, 359.

[114] Y. Jin, C. Hu, Q. Dai, Y. Xiao, Y. Lin, J. W. Connell, F. Chen, L. Dai, *Adv. Funct. Mater.* **2018**, *28*, 1804630.

[115] Z. Zhang, Z. Zhang, P. Liu, Y. Xie, K. Cao, Z. Zhou, *J. Mater. Chem. A* **2018**, *6*, 3218.

[116] S. X. Yang, P. He, H. S. Zhou, *Energy Environ. Sci.* **2016**, *9*, 1650.

[117] X. Hu, Z. Li, J. Chen, *Angew. Chem., Int. Ed. Engl.* **2017**, *56*, 5785.

[118] X. Wang, X. Zhang, Y. Lu, Z. Yan, Z. Tao, D. Jia, J. Chen, *ChemElectroChem* **2018**, *5*, 3628.

[119] X. Hu, P. H. Joo, E. Matios, C. Wang, J. Luo, K. Yang, W. Li, *Nano Lett.* **2020**, *20*, 7700.

[120] W. I. Al Sadat, L. A. Archer, *Sci. Adv.* **2016**, *2*, e1600968, .

[121] W. Ma, X. Liu, C. Li, H. Yin, W. Xi, R. Liu, G. He, X. Zhao, J. Luo, Y. Ding, *Adv. Mater.* **2018**, *30*, 1801152.

[122] R. Yang, J. Xie, Q. Liu, Y. Huang, J. Lv, M. A. Ghausi, X. Wang, Z. Peng, M. Wu, Y. Wang, *J. Mater. Chem. A* **2019**, *7*, 2575.

[123] K. Wang, Y. Wu, X. Cao, L. Gu, J. Hu, *Adv. Funct. Mater.* **2020**, *30*, 1908965.

[124] H.-J. Noh, S.-T. Myung, H.-G. Jung, H. Yashiro, K. Amine, Y.-K. Sun, *Adv. Funct. Mater.* **2013**, *23*, 1028.

[125] Z. Zhang, C. Yang, S. Wu, A. Wang, L. Zhao, D. Zhai, B. Ren, K. Cao, Z. Zhou, *Adv. Energy Mater.* **2019**, *9*, 1803096.

[126] J. Zhou, X. Li, C. Yang, Y. Li, K. Guo, J. Cheng, D. Yuan, C. Song, J. Lu, B. Wang, *Adv. Mater.* **2019**, *31*, 1804439.

[127] C. Yang, K. Guo, D. Yuan, J. Cheng, B. Wang, *J. Am. Chem. Soc.* **2020**, *142*, 6983.

[128] Y. Hou, J. Wang, L. Liu, Y. Liu, S. Chou, D. Shi, H. Liu, Y. Wu, W. Zhang, J. Chen, *Adv. Funct. Mater.* **2017**, *27*, 1700564.

[129] R. Yang, Z. Peng, J. Xie, Y. Huang, R. A. Borse, X. Wang, M. Wu, Y. Wang, *ChemSusChem* **2020**, *13*, 2621.

[130] X. Hu, J. Sun, Z. Li, Q. Zhao, C. Chen, J. Chen, *Angew. Chem.* **2016**, *128*, 6592.

[131] B. Scrosati, J. Garche, *J. Power Sources* **2010**, *195*, 2419.

ADVANCED
SCIENCE NEWS
www.advancedsciencenews.com

NANO · MICRO
small
www.small-journal.com

[132] T. Wang, X. Sang, W. Zheng, B. Yang, S. Yao, C. Lei, Z. Li, Q. He, J. Lu, L. Lei, L. Dai, Y. Hou, *Adv. Mater.* **2020**, *32*, 2002430.

[133] D. T. Whipple, P. J. A. Kenis, *J. Phys. Chem. Lett.* **2010**, *1*, 3451.

[134] J. Li, G. Chen, Y. Zhu, Z. Liang, A. Pei, C.-L. Wu, H. Wang, H. R. Lee, K. Liu, S. Chu, Y. Cui, *Nat. Catal.* **2018**, *1*, 592.

[135] X. Wang, J. F. de Araujo, W. Ju, A. Bagger, H. Schmies, S. Kuhl, J. Rossmeisl, P. Strasser, *Nat. Nanotechnol.* **2019**, *14*, 1063.

[136] F. N. Al-Rowaili, A. Jamal, M. S. Ba Shammakh, A. Rana, *ACS Sustainable Chem. Eng.* **2018**, *6*, 15895.

[137] K. P. Kuhl, T. Hatsukade, E. R. Cave, D. N. Abram, J. Kibsgaard, T. F. Jaramillo, *J. Am. Chem. Soc.* **2014**, *136*, 14107.

[138] a) M. Liu, Y. Pang, B. Zhang, P. De Luna, O. Voznyy, J. Xu, X. Zheng, C. T. Dinh, F. Fan, C. Cao, F. P. G. de Arquer, T. S. Safaei, A. Mepham, A. Klinkova, E. Kumacheva, T. Filleter, D. Sinton, S. O. Kelley, E. H. Sargent, *Nature* **2016**, *537*, 382; b) R. Shi, J. Guo, X. Zhang, G. I. N. Waterhouse, Z. Han, Y. Zhao, L. Shang, C. Zhou, L. Jiang, T. Zhang, *Nat. Commun.* **2020**, *11*, 3028.

[139] S. Sarfraz, A. T. Garcia-Esparza, A. Jedidi, L. Cavallo, K. Takanabe, *ACS Catal.* **2016**, *6*, 2842.

[140] H. Yang, Y. w. Hu, J. j. Chen, M. S. Balogun, P. p. Fang, S. Zhang, J. Chen, Y. Tong, *Adv. Energy Mater.* **2019**, *9*, 1803096.

[141] N. M. Markovic, P. N. Ross, *Surf. Sci. Rep.* **2002**, *45*, 117.

[142] A. A. Peterson, J. K. Nørskov, *J. Phys. Chem. Lett.* **2012**, *3*, 251.

[143] H. Yang, Y. Wu, G. Li, Q. Lin, Q. Hu, Q. Zhang, J. Liu, C. He, *J. Am. Chem. Soc.* **2019**, *141*, 12717.

[144] a) X. W. Nie, M. R. Esopi, M. J. Janik, A. Asthagiri, *Angew. Chem., Int. Ed.* **2013**, *52*, 2459; b) Z. Zhao, G. Lu, *J. Phys. Chem. C* **2019**, *123*, 4380.

[145] Z. L. Zhao, G. Lu, *J. Phys. Chem. C* **2019**, *123*, 4380.

[146] S. Zhao, S. Guo, C. Zhu, J. Gao, H. Li, H. Huang, Y. Liu, Z. Kang, *RSC Adv.* **2017**, *7*, 1376.

[147] J. Wu, Y. Huang, W. Ye, Y. Li, *Adv. Sci.* **2017**, *4*, 1700194.

[148] X. F. Bai, W. Chen, C. C. Zhao, S. G. Li, Y. F. Song, R. P. Ge, W. Wei, Y. H. Sun, *Angew. Chem., Int. Ed.* **2017**, *56*, 12219.

[149] W.-Y. Li, X. Zhao, J.-S. Dang, *J. Mater. Chem. A* **2019**, *7*, 13935.

[150] a) N. Han, P. Ding, L. He, Y. Li, Y. Li, *Adv. Energy Mater.* **2020**, *10*, 1902338; b) P. Lamagni, M. Miola, J. Catalano, M. S. Hvid, M. A. H. Mamakhel, M. Christensen, M. R. Madsen, H. S. Jeppesen, X.-M. Hu, K. Daasbjerg, T. Skrydstrup, N. Lock, *Adv. Funct. Mater.* **2020**, *30*, 1910408.

[151] H. Liu, J. Xia, N. Zhang, H. Cheng, W. Bi, X. Zu, W. Chu, H. Wu, C. Wu, Y. Xie, *Nat. Catal.* **2021**, *4*, 202.

[152] K. Fan, Y. Jia, Y. Ji, P. Kuang, B. Zhu, X. Liu, J. Yu, *ACS Catal.* **2020**, *10*, 358.

[153] a) C. Reller, R. Krause, E. Volkova, B. Schmid, S. Neubauer, A. Rucki, M. Schuster, G. Schmid, *Adv. Energy Mater.* **2017**, *7*, 1602114; b) C.-T. Dinh, T. Burdyny, M. G. Kibria, A. Seifitokaldani, C. M. Gabardo, F. P. García de Arquer, A. Kiani, J. P. Edwards, P. De Luna, O. S. Bushuyev, C. Zou, R. Quintero-Bermudez, Y. Pang, D. Sinton, E. H. Sargent, *Science* **2018**, *360*, 783.

[154] a) A. D. Handoko, C. W. Ong, Y. Huang, Z. G. Lee, L. Lin, G. B. Panetti, B. S. Yeo, *J. Phys. Chem. C* **2016**, *120*, 20058; b) Y. Kwon, Y. Lum, E. L. Clark, J. W. Ager, A. T. Bell, *ChemElectroChem* **2016**, *3*, 1012.

[155] D. Gao, I. Sinev, F. Scholten, R. M. Aran-Ais, N. J. Divins, K. Kvashnina, J. Timoshenko, B. R. Cuenya, *Angew. Chem., Int. Ed. Engl.* **2019**, *58*, 17047.

[156] F. P. García de Arquer, C.-T. Dinh, A. Ozden, J. Wicks, C. McCallum, A. R. Kirmani, D.-H. Nam, C. Gabardo, A. Seifitokaldani, X. Wang, Y. C. Li, F. Li, J. Edwards, L. J. Richter, S. J. Thorpe, D. Sinton, E. H. Sargent, *Science* **2020**, *367*, 661.

[157] a) A. R. Paris, A. B. Bocarsly, *Faraday Discuss.* **2019**, *215*, 192; b) N. S. Romero Cuellar, K. Wiesner-Fleischer, M. Fleischer, A. Rucki, O. Hinrichsen, *Electrochim. Acta* **2019**, *307*, 164.

[158] K. U. D. Calvinho, A. B. Laursen, K. M. K. Yap, T. A. Goetjen, S. Hwang, N. Murali, B. Mejia-Sosa, A. Lubarski, K. M. Teeluck, E. S. Hall, E. Garfunkel, M. Greenblatt, G. C. Dismukes, *Energy Environ. Sci.* **2018**, *11*, 2550.

[159] C. Chen, J. F. Khosrowabadi Kotyk, S. W. Sheehan, *Chem* **2018**, *4*, 2571.

[160] O. G. Sánchez, Y. Y. Birdja, M. Bulut, J. Vaes, T. Breugelmans, D. Pant, *Curr. Opin. Green Sustainable Chem.* **2019**, *16*, 47.

[161] T. S. Matthews, M. Kaplun, Z. Liu, Q. Chen, R. Kutz, S. Luopa, K. Lewinski, R. I. Masel, *Meeting Abstracts, The Electrochemical Society* **2015**, *1717*, https://iopscience.iop.org/article/10.1149/MA2015-01/30/1717.

[162] R. Küngas, P. Blennow, T. Heiredal-Clausen, T. Holt, J. Rass-Hansen, S. Primdahl, J. B. Hansen, *ECS Trans.* **2017**, *78*, 2879.

[163] R. Krause, D. Reinisch, C. Reller, H. Eckert, D. Hartmann, D. Taroata, K. Wiesner-Fleischer, A. Bulan, A. Lueken, G. Schmid, *Chem. Ing. Tech.* **2020**, *92*, 53.

[164] R. I. Masel, Z. Liu, H. Yang, J. J. Kaczur, D. Carrillo, S. Ren, D. Salvatore, C. P. Berlinguette, *Nat. Nanotechnol.* **2021**, *16*, 118.

[165] N. S. Romero Cuellar, C. Scherer, B. Kaçkar, W. Eisenreich, C. Huber, K. Wiesner-Fleischer, M. Fleischer, O. Hinrichsen, *J. CO2 Util.* **2020**, *36*, 263.

[166] T. Haas, R. Krause, R. Weber, M. Demler, G. Schmid, *Nat. Catal.* **2018**, *1*, 32.

[167] J.-L. Bertaux, O. Korablev, S. Perrier, E. Quémerais, F. Montmessin, F. Leblanc, S. Lebonnois, P. Rannou, F. Lefèvre, F. Forget, A. Fedorova, E. Dimarellis, A. Reberac, D. Fonteyn, J. Y. Chaufray, S. Guibert, *J. Geophys. Res.* **2006**, *111*.

[168] D. H. Deng, K. S. Novoselov, Q. Fu, N. F. Zheng, Z. Q. Tian, X. H. Bao, *Nat. Nanotechnol.* **2016**, *11*, 218.

[169] Y. Zhu, W. Peng, Y. Li, G. Zhang, F. Zhang, X. Fan, *Small Methods* **2019**, *3*, 1800438.

[170] W. Luo, W. Xie, M. Li, J. Zhang, A. Züttel, *J. Mater. Chem. A* **2019**, *7*, 4505.

[171] Y. Cheng, S. Yang, S. P. Jiang, S. Wang, *Small Methods* **2019**, *3*, 1800440.

[172] L. Zhang, H. Liu, S. Liu, M. Norouzi Banis, Z. Song, J. Li, L. Yang, M. Markiewicz, Y. Zhao, R. Li, M. Zheng, S. Ye, Z.-J. Zhao, G. A. Botton, X. Sun, *ACS Catal.* **2019**, *9*, 9350.

[173] H. A. Hansen, J. B. Varley, A. A. Peterson, J. K. Norskov, *J. Phys. Chem. Lett.* **2013**, *4*, 388.

[174] A. D. Handoko, F. Wei, B. S. Y. Jenndy, Z. W. Seh, *Nat. Catal.* **2018**, *1*, 922.

[175] D. Gao, R. M. Arán-Ais, H. S. Jeon, B. R. Cuenya, *Nat. Catal.* **2019**, *2*, 198.

[176] J. Wang, S. Kattel, C. J. Hawxhurst, J. H. Lee, B. M. Tackett, K. Chang, N. Rui, C. J. Liu, J. G. Chen, *Angew. Chem., Int. Ed. Engl.* **2019**, *58*, 6271.

[177] K. Yang, R. Kas, W. A. Smith, *J. Am. Chem. Soc.* **2019**, *141*, 15891.

[178] E. C. Neyts, K. K. Ostrikov, M. K. Sunkara, A. Bogaerts, *Chem. Rev.* **2015**, *115*, 13408.

[179] a) X. Tu, J. C. Whitehead, *Appl. Catal., B* **2012**, *125*, 439; b) L. Wang, Y. Zhao, C. Liu, W. Gong, H. Guo, *Chem. Commun.* **2013**, *49*, 3787.

[180] a) F. Liang, T. Shimizu, M. Tanaka, S. Choi, T. Watanabe, *Diamond Relat. Mater.* **2012**, *30*, 70; b) F. Liang, T. Shimizu, M. Tanaka, S. Choi, T. Watanabe, *Jpn. J. Appl. Phys.* **2013**, *52*, 126601; c) F. Liang, M. Tanaka, S. Choi, T. Watanabe, *J. Chem. Eng. Jpn.* **2014**, *47*, 296; d) F. Liang, M. Tanaka, S. Choi, T. Watanabe, *Mater. Res. Bull.* **2014**, *60*, 158; e) F. Liang, M. Tanaka, S. Choi, T. Watanabe, *J. Phys. D: Appl. Phys.* **2016**, *49*, 125201; f) F. M. Su, X. C. Qiu, F. Liang, M. Tanaka, T. Qu, Y. C. Yao, W. H. Ma, B. Yang, Y. N. Dai, K. Hayashi, T. Watanabe, *Nanomaterials* **2018**, *8*, 684; g) D. Zhang, K. Ye, Y. C. Yao, F. Liang, T. Qu, W. H. Ma, B. Yang, Y. N. Dai, T. Watanabe, *Carbon* **2019**, *142*, 278; h) N. Jiang, C. Qiu, L. Guo, K. Shang, N. Lu, J. Li, Y. Zhang, Y. Wu, *J. Hazard. Mater.* **2019**, *369*, 611; i) Y. X. Zeng, L. Wang, C. F. Wu, J. Q. Wang, B. X. Shen, X. Tu, *Appl. Catal., B* **2018**, *224*, 469.

ADVANCED
SCIENCE NEWS

www.advancedsciencenews.com

NANO · MICRO
small
www.small-journal.com

[181] Y. W. Choi, F. Scholten, I. Sinev, B. R. Cuenya, *J. Am. Chem. Soc.* **2019**, *141*, 5261.

[182] A. Yada, K. Nagata, Y. Ando, T. Matsumura, S. Ichinoseki, K. Sato, *Chem. Lett.* **2018**, *47*, 284.

[183] A. F. Zahrt, J. J. Henle, B. T. Rose, Y. Wang, W. T. Darrow, S. E. Denmark, *Science* **2019**, *363*, eaau5631.

[184] J. G. Freeze, H. R. Kelly, V. S. Batista, *Chem. Rev.* **2019**, *119*, 6595.

[185] a) K. Tran, Z. W. Ulissi, *Nat. Catal.* **2018**, *1*, 696; b) M. Zhong, K. Tran, Y. Min, C. Wang, Z. Wang, C. T. Dinh, P. De Luna, Z. Yu, A. S. Rasouli, P. Brodersen, S. Sun, O. Voznyy, C. S. Tan, M. Askerka, F. Che, M. Liu, A. Seifitokaldani, Y. Pang, S. C. Lo, A. Ip, Z. Ulissi, E. H. Sargent, *Nature* **2020**, *581*, 178.

[186] Z. Xie, X. Zhang, Z. Zhang, Z. Zhou, *Adv. Mater.* **2017**, *29*, 1605891.

[187] P. Bai, J. Li, F. R. Brushett, M. Z. Bazant, *Energy Environ. Sci.* **2016**, *9*, 3221.

[188] a) J. C. Bachman, S. Muy, A. Grimaud, H. H. Chang, N. Pour, S. F. Lux, O. Paschos, F. Maglia, S. Lupart, P. Lamp, L. Giordano, Y. Shao-Horn, *Chem. Rev.* **2016**, *116*, 140; b) M. Hou, F. Liang, K. Chen, Y. Dai, D. Xue, *Nanotechnology* **2020**, *31*, 132003.

[189] a) L. Fan, S. Wei, S. Li, Q. Li, Y. Lu, *Adv. Energy Mater.* **2018**, *8*, 1702657; b) C. Xia, P. Zhu, Q. Jiang, Y. Pan, W. Liang, E. Stavitsk, H. N. Alshareef, H. Wang, *Nat. Energy* **2019**, *4*, 776.

[190] J. Yu, Y. S. Hu, F. Pan, Z. Zhang, Q. Wang, H. Li, X. Huang, L. Chen, *Nat. Commun.* **2017**, *8*, 14629.

[191] F. Liang, X. Qiu, Q. Zhang, Y. Kang, A. Koo, K. Hayashi, K. Chen, D. Xue, K. N. Hui, H. Yadegari, X. Sun, *Nano Energy* **2018**, *49*, 574.

[192] J. J. Carroll, J. D. Slupsky, A. E. Mather, *J. Phys. Chem. Ref. Data* **1991**, *20*, 1201.

[193] M. G. Kibria, J. P. Edwards, C. M. Gabardo, C.-T. Dinh, A. Seifitokaldani, D. Sinton, E. H. Sargent, *Adv. Mater.* **2019**, *31*, 1807166.

[194] T. N. Nguyen, C.-T. Dinh, *Chem. Soc. Rev.* **2020**, *49*, 7488.

[195] C. Xia, P. Zhu, Q. Jiang, Y. Pan, W. Liang, E. Stavitski, H. N. Alshareef, H. Wang, *Nat. Energy* **2019**, *4*, 776.

Feng Liang is a full professor in Kunming University of Science and Technology and a visiting professor of Kyushu University in Japan. Dr. Liang received his Ph.D. in Environmental Chemistry in 2014 from Tokyo Institute of Technology, Japan. From 2014 to 2015, he worked as a postdoc at Tokyo Institute of Technology. His current research interests are focused on metal–air/CO_2 batteries, solid-state batteries, plasma preparation and modification nanomaterials and their application for electrochemical energy storage and conversion.

Kaiwen Zhang received his B.S. degree in metallurgy engineering in 2020 from Kunming University of Science and Technology. Zhang is currently a Master's student in the Department of Chemical Engineering of Kyushu University, under the supervisor of Prof. Takayuki Watanabe. His research interests include synthesis of nanoparticles with thermal plasma and catalysts applied on metal–CO_2 batteries.

Lei Zhang received his B.S. degree in Chemistry in 2008 and Ph.D. degree in Nanomaterial Chemistry in 2014 from Xiamen University with Prof. Zhaoxiong Xie. He was a visiting graduate student at Georgia Institute of Technology in Prof. Younan Xia's group from 2012 to 2014. From 2015 to 2016, he worked as a postdoc at Collaborative Innovation Center of Chemical Science and Engineering in Tianjin University. He is currently a postdoctoral associate with Professor Xueliang Sun at University of Western Ontario. His research interests include the design and synthesis of metal nanomaterials and single-atom catalysts for fuel cells, carbon dioxide reduction, and water splitting devices.

Yingjie Zhang is a University Committee chair and full professor of Kunming University of Science and Technology. Prof. Zhang worked as senior visiting scholar at University of Manchester from 1997 to 1998 and received her Ph.D. in nonferrous metal metallurgy from Kunming University of Science and Technology in 1999. Her research interests are focused on electrochemical energy; electrochemical corrosion and protection; electrochemical environmental protection.

Yong Lei is professor and head of group (Chair) of Applied Nano-Physics at Technical University of Ilmenau in Germany. He started to work in Germany as an Alexander von Humboldt Fellow at Karlsruhe Institute of Technology in 2003. From 2006 he worked at University of Muenster as a group leader and Junior Professor. In 2011, he joined the Technical University of Ilmenau as a professor. His research focuses on template-based nanostructuring, energy conversion and storage devices, and optoelectronic applications of functional nanostructures. He received a few prestigious funding in Europe and Germany such as two European Research Council Grants.

Xueliang (Andy) Sun is a Canada Research Chair in Development of Nanomaterials for Clean Energy, Fellow of the Royal Society of Canada and Canadian Academy of Engineering and full professor at the University of Western Ontario, Canada. Dr. Sun received his Ph.D. in materials chemistry in 1999 from the University of Manchester, UK, which he followed up by working as a postdoctoral fellow at the University of British Columbia, Canada and as a research associate at L'Institut National de la Recherche Scientifique (INRS), Canada. His current research interests are focused on advanced materials for electrochemical energy storage and conversion, including solid-state batteries, solid-state electrolytes, Li–S batteries, metal–air batteries, single atom catalysts and low temperature fuel cells.